NEUROPROTECTION AFTER TRAUMATIC SPINAL CORD INJURY THROUGH MITOCHONDRIAL CALCIUM UNIPORTER INHIBITION

By

Kennedy Brittain

Submitted in partial fulfillment of the requirements for

the degree of Master of Science
at

Dalhousie University
Halifax, Nova Scotia

July, 2022

Table of Contents

LIST OF FIGURES ..... **iv**

ABSTRACT ..... **vi**

ABBREVIATIONS ..... **vii**

ACKNOWLEDGMENTS ..... **ix**

1.0 INTRODUCTION **1**

1.1 Spinal Cord Injury (SCI) 1

1.2 The Spinal Cord: General Anatomy 2

1.3 Stages of Spinal Cord Injury 6

1.4 Secondary Spinal Cord Injury (sSCI) 8

1.5 The Role of Mitochondria in Neuroprotection 15

1.6 The Mitochondrial Calcium Uniporter 16

1.7 Ruthenium 265 and Neuroprotection 18

1.8 Contusion SCI & Animal Model 20

1.9 Study Objectives 21

2.0 LOCAL DELIVERY OF RU265 BY EPIDURAL APPLICATION FOLLOWING TRAUMATIC SPINAL CORD INJURY: OPTIMIZATION AND EFFICACY **23**

2.1 Introduction 24

2.2 Methods 25

2.2.1 Animals 25

2.2.2 Experimental Spinal Cord Injury 25

2.2.3 Dose Determination & Epidural Delivery 27

2.2.4 Tissue Collection 29

2.2.5 Inductively Coupled Plasma Mass Spectrometry (ICP-MS) Sample Preparation 30

2.2.6 ICP-MS Analysis 31

2.3 Results 32

2.4 Discussion 37

3.0 AN INVESTIGATION OF THE MITOPROTECTIVE AND NEUROPROTECTIVE PROPERTIES OF RU265 FOLLOWING tSCI **40**

3.1 Introduction 41

3.2 Methods 42

3.2.1 Electron Microscopy Sample Preparation 42

3.2.2 Transmission Electron Microscopy 42

3.2.3 TEM Mitochondria Analysis 43

3.2.4 Fluoro-Jade C and Immunohistochemistry Sample Preparation & Processing 44

3.2.5 Fluoro-Jade C & Hoechst Labelling 45
3.2.6 Double Labelling with FJC & NeuN Immunolabelling 46
3.2.7 FJC Imaging and Analysis 47
3.3 Results 48
3.3.1 Evaluation of Impact Parameters 48
3.3.2 Evaluation of Mitochondrial Structural Integrity following tSCI 48
3.3.3 NeuN Immunolabelling 54
3.3.4 Evaluation of Neurodegeneration with Fluoro-Jade C Labelling 55
3.4 Discussion 57
4.0 GENERAL DISCUSSION 59
4.1 Local delivery of Ru265 by Epidural Application 59
4.2 Mitoprotective and Neuroprotective effects of Ru265 62
4.3 Conclusions 65
BIBLIOGRAPHY 66
APPENDIX 77

LIST OF FIGURES

Figure 1: Cross-sectional anatomy of the spinal cord and nerve roots.. 4
Figure 2: Superior view of the components of a typical human vertebra. 5
Figure 3: Glutamate excitotoxicity initiated by tSCI.. 10
Figure 4: The intrinsic pathway of apoptosis..... 12
Figure 5: The reactive oxygen species producing Fenton and Haber-Weiss reactions..... 14
Figure 6: A schematic of the current model of the MCU complex 18
Figure 7: Experimental set-up for delivery of a tSCI. 27
Figure 8: A schematic of epidural drug delivery to the spinal cord. 28
Figure 9: Ru265 concentrations in the spinal cord parenchyma following intraperitoneal and epidural delivery 33
Figure 10: Ru265 concentrations in the forebrain following tSCI delivered epidurally and by IP injection..... 34
Figure 11: Ru265 concentrations from whole blood following tSCI delivered epidurally and by IP injection 35
Figure 12: Combined graph of Ru265 concentrations from spinal cord (SC), brain (Br), and whole blood (Bl) following tSCI delivered epidurally and by IP injection. 36
Figure 13: An injured spinal cord 4 hours post-impact isolated by serial laminectomy.. 45
Figure 14: A spinal cord section indicating the region of interest for counting FJC + Cells. 47
Figure 15: Scale of mitochondrial degradation following tSCI. 49
Figure 16: Electron micrographs of control and Ru265 treated SC sections 4h following tSCI..50
Figure 17: Number of healthy mitochondria in control versus treatment samples 4h following tSCI.. 51
Figure 18: Number of damaged mitochondria in control versus treatment samples 4h following tSCI.. 52
Figure 19: Number of healthy and damaged mitochondria in control versus treatment samples counted by secondary individual. 53
Figure 20. Fluorescence microscopy showing colocalization of FJC, Hoechst, and NeuN.. 54
Figure 21. Fluorescence images of a control and Ru265 treated SC section 55
Figure 22: Degenerating neurons in treatment versus control samples 72h following tSCI.. 56

Figure 23: Impact parameters of control and Ru265 treated mice. 77
Figure 24: Force values of control and Ru265 treated animals 78
Figure 25: Displacement values of control and Ru265 treated animals.....78
Figure 26: Histology of injured spinal cord sections in control and Ru265 treated specimens...79

ABSTRACT

A common final pathway of secondary spinal cord injury (sSCI) is glutamate excitotoxicity, manifested by calcium (Ca^{2+}) overloading of the neuron. Mitochondria are damaged by excessive intake of cytoplasmic Ca^{2+} through the mitochondrial calcium uniporter (MCU). When this occurs, the mitochondria become overwhelmed, collapse, and trigger neuronal cell death. We hypothesized that MCU inhibition by Ru265 will improve recovery after traumatic spinal cord injury (tSCI) by preserving mitochondrial integrity and function essential for axonal survival and repair. We demonstrated that intraperitoneal (IP) delivery at a dose previously shown to be neuroprotective in a stroke model (3 mg/kg) promotes seizure activity in mice, prompting us to investigate more localized methods of drug delivery and a lower total dose. We compared single epidural and IP doses of Ru265 (1 mg/kg; non seizure inducing dose, determined empirically), in mice immediately after a tSCI. Mice were sampled 4, 8 and 24 hours afterwards and Ru265 levels within the spinal parenchyma, forebrain, and whole blood determined using mass spectrometry (MS). MS data supports that Ru265 reached higher concentrations in the spinal parenchyma with epidural application (over the lesion), than via IP injection. This effect was also time-dependent with the drug concentration increasing with time. Epidural application was determined to be a feasible and effective method of Ru265 delivery. Following this, mitochondrial integrity of Ru265 treated and control mice was evaluated with transmission electron microscopy. Evaluation of the structural integrity of mitochondria following tSCI revealed that there were significantly more healthy mitochondria ($p<0.0001$) and significantly fewer damaged mitochondria ($p<0.0001$) in the Ru265 treated sections compared to control specimens. To determine if this increase in mitochondrial preservation translated to improved neuronal survival, Fluoro-Jade C, a fluorescent label for degenerating neurons was used. Samples treated with Ru265 had significantly fewer degenerating neurons compared to controls ($p=0.009$) suggesting that Ru265 may improve neuronal survival following tSCI. These findings support that Ru265 provides mitoprotection and as a likely result, neuroprotection following tSCI. To our knowledge this is the first study demonstrating the benefits of MCU inhibition in the context of SCI.

ABBREVIATIONS

Abbreviation	Expansion
ADP	Adenosine diphosphate
AMPA	α-amino-3-hydroxy-5-methyl-4-isoxazolepropionic acid
ANOVA	Analysis of variance
ATP	Adenosine triphosphate
BAX	BCL2 associated X
BBB	Basso-Beattie-Bresnahan
BMS	Basso mouse scale
BSA	Bovine serum albumin
BSCB	Blood-spinal cord barrier
Ca^{2+}	Calcium
CNS	Central nervous system
CSF	Cerebral spinal fluid
DCML	Dorsal-column medial lemniscus
DNA	Deoxyribonucleic acid
DRG	Dorsal root ganglion
EM	Electron microscopy
EMRE	Essential MCU regulator
ER	Endoplasmic reticulum
ETC	Electron transport chain
FJC	Fluoro-Jade C
HI	Hypoxia/ischemia
ICP	Inductively coupled plasma
IMM	Inner mitochondrial membrane
IP	Intraperitoneal
MCU	Mitochondrial calcium uniporter
MICU	Mitochondrial calcium uptake
MS	Mass spectrometry
NMDA	N-methyl-D-aspartate
NSAID	Non-steroidal anti-inflammatory drugs
OGD	Oxygen-glucose deprivation
PBS	Phosphate-buffered saline
PFA	Paraformaldehyde
mPTP	Mitochondrial permeability transition pore
ROS	Reactive oxygen species

Abbreviation	Expansion
SC	Spinal cord
SCI	Spinal cord injury
sSCI	Secondary spinal cord injury
TBI	Traumatic brain injury
TEM	Transmission electron microscopy
tSCI	Traumatic spinal cord injury
VDAC	Voltage-dependant anion channel
YFP	Yellow fluorescent protein

ACKNOWLEDGMENTS

Firstly, I would like to thank my supervisor Dr. Sean Christie for his guidance, mentorship, and encouragement throughout the duration of this project. I would also like to extend my thanks to Dr. Saranyan Pillai (Research Associate) who contributed immensely to shaping this work. Without his generous guidance, teaching several techniques used throughout this thesis and invaluable advice, this work would not have been possible.

Likewise, thank you to the other members of my advisory committee Dr. Kazue Semba, Dr. James Fawcett, and Dr. Ying Zhang for their great feedback and support throughout this project.

Furthermore, I wish to acknowledge my thanks to Dr. George Robertson and the entire Robertson lab for their collaboration and providing me with Ru265. In particular, I would like to thank Robyn Novorolsky for never hesitating to provide me with more Ru265 (no matter how many times I asked). I would also like to thank Kaitlyn Fraser for agreeing to be the second individual to confirm my mitochondria counting. The hours she put into counting and organizing this part of the data are extremely appreciated. Finally, I thank Gracious Kasheke for his support and advice throughout the duration of this work.

I remain very thankful for members of the Health and Environmental Research Centre (HERC), in particular Dr. Jong Sung Kim and Erin Keltie for their assistance with mass spectrometry. Additionally, I would like to thank Mary-Ann Trevors and Brianne Lindsay for their expertise and training in electron and fluorescence microscopy, respectively.

I would also like to acknowledge my gratitude to CIHR, the Department of Surgery, and the Department of Medical Neuroscience of Dalhousie University for graduate student and research funding.

Lastly, I would like to thank my family, friends, and partner Andrew for their unconditional support during this project. Their continued encouragement was paramount to the completion of this project.

1.0 INTRODUCTION

1.1 Spinal Cord Injury (SCI)

In 2019, the estimated number of persons suffering from spinal cord injury (SCI) in Canada was over 86 000 (Praxis Spinal Cord Institute, 2021). Of this number, 51% represented traumatic spinal cord injuries (tSCI) which occur due to motor vehicle accidents, falls, sports injuries, etc. (Noonan et al., 2012). More specifically, tSCI results from the abrupt transfer of an external mechanical force(s) that disrupts the SC cellular architecture, as opposed to non-traumatic SCI's, which result from insidious, progressive compression secondary to tumours, infections, vascular insults, and degenerative diseases (Alizadeh et al., 2019). Historically, SCI demographics suggest that 78% of tSCIs occur in males aged 16-34 years (NSCISC, 2019), however, more recently the gender difference is closing and an older population is represented (Praxis Spinal Cord Institute, 2021). Despite this, it remains that the majority of patients suffering from SCI have a significant portion of their lives ahead of them and, as a result, there is a considerable economic burden associated with their care ranging from $1.6-$5 million USD, depending on the severity of the injury (National Spinal Cord Injury Statistical Centre, 2019).

Traumatic spinal cord injury is a debilitating and devastating condition that impairs both the physical and emotional well-being affected individuals (Post and van Leeuwen, 2012). In addition to impaired ambulation, patients suffering from tSCI often experience respiratory, gastrointestinal, urological, and sexual dysfunction, among several other secondary complications (Sezer et al., 2015). These impairments often leave tSCI patients dependent on others for lifelong support and cause significant barriers in numerous aspects of their lives (Sezer et al., 2015). The severity of SCI and ultimate patient outcomes correspond with the anatomical

segment of the SC that is injured and typically give rise to sensory and/or motor impairments below the level of injury (Roberts et al., 2017; Alizadeh et al., 2019). Higher injuries (e.g. to the cervical region) can cause tetraplegia, whereas lower injuries (e.g. to the thoracic region) may only cause paraplegia (Roberts et al., 2017).

SCIs are commonly classified into two different phases termed primary and secondary SCI (sSCI) (Alizadeh et al., 2019). The primary injury results from the damage caused by the initial mechanical trauma to the SC, whereas the term secondary injury is meant to reflect a series of deleterious biochemical and physiological reactions which occur in response to the primary insult (Hilton et al., 2017). Secondary injury results in further death of neurons and supporting cells, translating to a progression in sensory and motor deficits (Lu et al., 2000). For this reason, it is imperative to investigate therapeutics that maximize neuroprotection following SCI. sSCI begins within minutes of the primary injury and may persist for weeks, and even months, following the initial impact to the SC (Alizadeh et al., 2019). While there are no feasible treatments for primary SCI, apart from prevention, due to the prolonged duration of sSCI there is opportunity for researchers to develop pharmacological interventions to promote neuroprotection during this time. To understand SCI further, we must first investigate the anatomy of the spinal cord.

1.2 The Spinal Cord: General Anatomy

The spinal cord (SC) or medulla spinalis comprises one of two primary components of the central nervous system (CNS). It extends caudally from the medulla oblongata of the brain and is encapsulated by the bony vertebral column, which serves as physical protection. It can be divided longitudinally into the cervical, thoracic, lumbar, sacral, and coccygeal regions (Watson

and Kayalioglu, 2009). Similar to the brain, the SC is enclosed by three meningeal layers from the outermost to innermost: the dura, arachnoid, and pia mater (Kayalioglu, 2009). The pia mater extends caudally from the conus medullaris to the coccyx forming the filum terminale, where it functions to anchor the SC to the vertebral column (Kayalioglu, 2009).

The SC primarily functions to transmit sensory, motor, and autonomic function throughout the body (Sengul and Watson, 2012; Carlson, 2014). Looking at the cross-sectional anatomy of the SC (Figure 1), the gray matter, often described as having an 'H' or 'butterfly' appearance in shape, is located centrally (Nógrádi and Vrbová, n.d.). The left and right regions of the gray matter are connected by the gray commissure which surrounds the central canal which contains cerebrospinal fluid (CSF) (Thau et al., 2021). The fourth ventricle remains in continuity with the central canal comprising the intraaxial CSF pathway. The anterior and posterior regions of gray matter are referred to as the ventral and dorsal horns, respectively (Cramer, 2014). The ventral horn contains both alpha and gamma motor neurons, in addition to spinal interneurons (Stifani, 2014). Cell bodies of the motor neurons in the ventral horn project axons through the ventral root, terminating in striated muscles (Purves et al., 2001). The dorsal root ganglion (DRG) is where the cell bodies of sensory neurons are found which project into the dorsal root entry zone. Both ventral and dorsal roots extend from the lateral sides of the SC and join to form the spinal nerves, and therefore spinal nerves have both sensory and motor function (Murray et al., 2003).

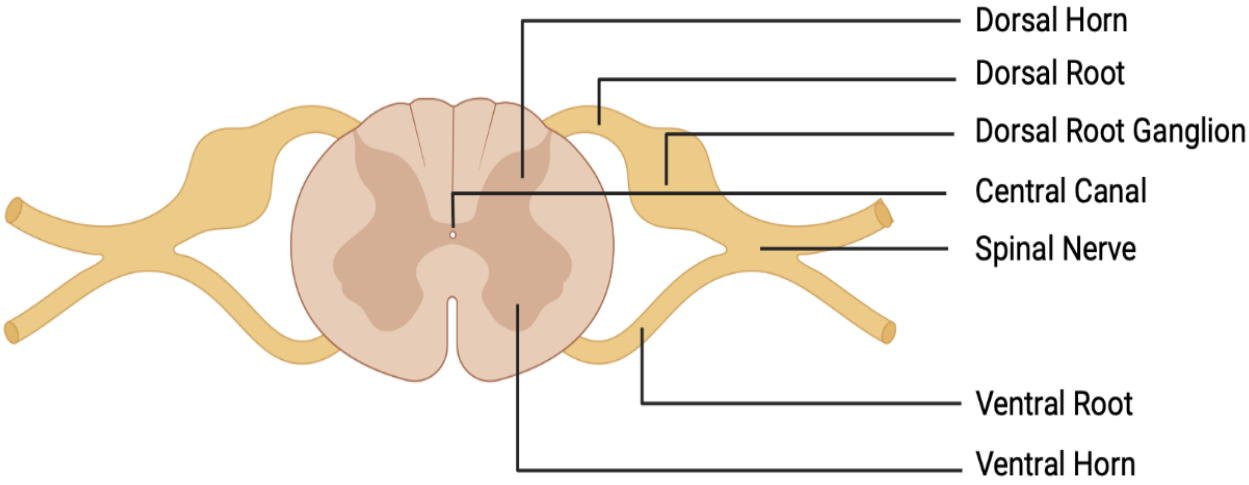

Figure 1*:* Cross-sectional anatomy of the spinal cord and nerve roots. Image created by Kennedy Brittain using Biorender, 2022.

Humans typically have 33 vertebrae which are connected by ligaments and intervertebral discs (Kayalioglu, 2009). The vertebra themselves consist of the load-bearing vertebral body (centrum) which supports body weight (Little, 2019). The other anatomically significant portion of the vertebra is the vertebral arch (Little, 2019). The vertebral arch is comprised of several structures including pedicles, lamina, inferior articular, superior articular, transverse and spinous processes (Figure 2) (Waxenbaum et al., 2021). The lamina of the vertebrae are bony plates extending dorsally from the pedicles, which are attached to the posterior portion of the vertebral body (Shanti et al., 2007; Waxenbaum et al., 2021). Within the cervical region the laminae are long and thick, whereas in the thoracic and lumbar they are short, and fused within the sacral region (Xu et al., 1999). Protruding dorsally from the laminae are the spinous processes, which serve as attachment points for various muscles and ligaments (Cramer, 2014). Their size and shape vary greatly across the regions of the vertebral column, going from shorter and thinner in the cervical region to taller and thicker in the lumbar region (Xu et al., 1999). The transverse processes, lateral extensions from the junction of the pedicles and laminae, serve as attachment

sites for muscles and also articulate with the ribs in the thoracic region (Maynard and Downes, 2019). The muscles attached to the transverse processes help to regulate posture and allow for rotation and lateral flexion of both single vertebrae and the entire spinal column (Cramer, 2014).

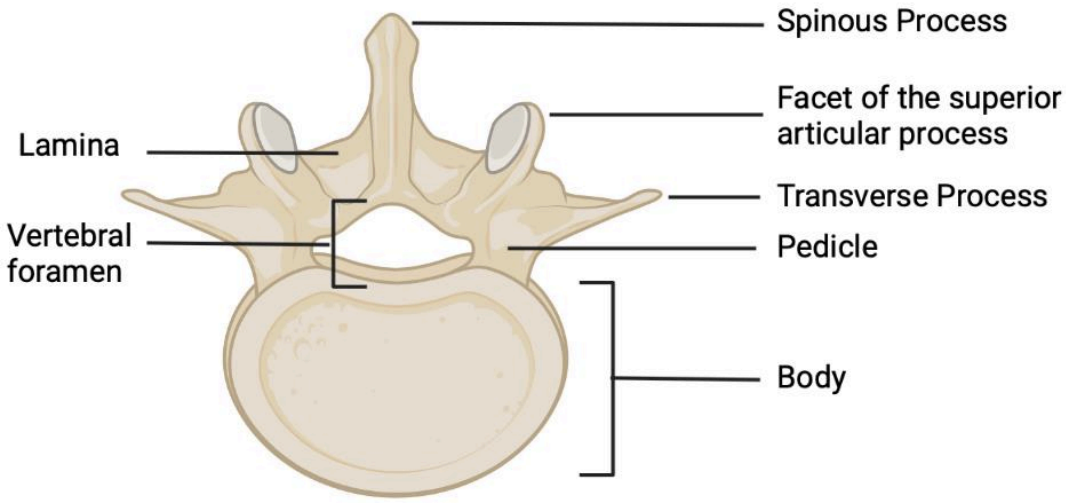

Figure 2: Superior view of the components of a typical human vertebra. These structures serve to protect the spinal cord and nerve roots. Image created by Kennedy Brittain using BioRender, 2022.

Generally, the anatomical layout of the spinal cord as previously described is similar between humans and rodents, making them a popular model for studying SCI (Cheriyan et al., 2014). A significant advantage to using mouse models to study SCI is that they closely mimic the general progression of injury, particularly in contusion models (Sharif-Alhoseini et al., 2017). For this reason, mice are increasingly used in order to study the basic cellular and molecular biology of SCI (Sharif-Alhoseini et al., 2017). However, there are some notable differences to be aware of. The major difference anatomically is the size and mass of the SC. In humans the average length of the SC is ~44cm whereas in mice it is ~2cm , and the weight of the human SC is ~28 g whereas in mice is 0.13 g (Roderick et al., 1973). Furthermore, mice have 25-30 vertebrae (7 cervical, 13 thoracic, 6 lumbar, and 4 sacral) (Sengul and Watson, 2012). The white

and gray matter distribution is very similar between human and rodents, as well as the location of the tracts (Watson and Harrison, 2012). One major exception, however, is the corticospinal tract which is in the ventral portion of the dorsal funiculus. In humans the majority of corticospinal tract fibers are found in the dorsal region of the lateral funiculus (Watson and Harrison, 2012). Despite these differences, in general the neuroanatomy and physiological processes within the SC are similar between humans and mice making them a valuable animal model for SCI research (Sharif-Alhoseini et al., 2017).

1.3 Stages of Spinal Cord Injury

With a better understanding of spinal cord anatomy, the distinct phases of SCI can be discussed. The temporal course of SCI is broadly divisible into three defined phases: acute, sub-acute, and chronic. There are several instances where the events in these phases overlap one another but each has characteristics that make them distinct.

Acute Phase

The acute phase of SCI consists of the physiological events that occur seconds to minutes following the primary injury (Ahuja et al., 2017). It comprises the initial physical trauma to the SC and the initiation of secondary injury cascades (Anjum et al., 2020). Systemically, there are widespread changes including hypotension, shock, and vasodilation (Popa et al., 2010). Neurons and glial cells, particularly oligodendrocytes, within the region of the impact are injured and undergo necrotic cell death (Almad et al., 2011). Secondary injury cascades begin and include pro-apoptotic signalling, glutamate-mediated excitotoxicity, ROS formation, inflammation, and ischemia due to disruptions in the microcirculation of the SC (Oyinbo, 2011). All of the events that occur in the acute phase progress into the sub-acute phase (Oyinbo, 2011).

Sub-Acute Phase

The sub-acute phase includes a continuation of some of the same events described in the acute phase of the injury (Ahuja et al., 2017). These events include shifts in ion homeostasis, edema, and necrotic cell death (Ahuja et al., 2017). However, as time passes new secondary injury mechanisms begin, such as immune system activation, and apoptotic cell death (Anjum et al., 2020). Several of these manifestations may initiate others, inducing a deleterious cycle of damaging events further increasing cell death. In addition, there is demyelination of axons (caused by death of oligodendrocytes), Wallerian degeneration (the active process of retrograde degeneration beginning at the distal end of the axon following injury), and the beginnings of the formation of a glial scar (composed of reactive glia in response to inflammation) surrounding the lesion (Buss et al., 2005; Yang et al., 2020). Events that distinguish this phase from others include free radical production, lipid peroxidation, energy failure and diminished ATP supply, and immune cell invasion (Oyinbo, 2011),

Chronic Phase

The chronic phase of SCI (months to years following injury) is characterized by the formation of a cystic cavity (syringomyelia), continued cell death, and glial scar maturation (Rowland et al., 2008). Syringomyelia is a fluid-filled cavity that may develop and contributes to injury progression by increasing compression of the SC (Jones, 2017). The pathophysiology is thought to involve ongoing inflammatory responses that initiate edema in the cord, ischemia, or swelling of the arachnoid mater (Jones, 2017). These lead to impaired CSF circulation in the central canal or subarachnoid space, which contributes to the enlargement of the cavity (Schwartz et al., 1999). It is also only during the chronic phase that axons begin the process of regeneration (Lu et al., 2007).

1.4 Secondary Spinal Cord Injury (sSCI)

sSCI begins within minutes of the primary injury and persists for months and in some cases even years after the initial impact to the SC. Secondary damage causes progressive deterioration of the spinal cord tissue surrounding the injury site. Now that the three primary phases of SCI have been established, the secondary injury mechanisms that occur during these phases will be reviewed in further detail.

Glutamate Excitotoxicity

Glutamate is the primary excitatory neurotransmitter within the CNS. In the neuron, it is synthesized by the endoplasmic reticulum and subsequently transported to the Golgi apparatus for further processing (Zhou and Danbolt, 2014). Once packaged within a vesicle, glutamate is transported down the axon via microtubules by way of a process termed anterograde transport (Vandenberg and Ryan, 2013). Anterograde motion is mediated by a motor protein called motor kinesin and is heavily dependent upon mitochondria to provide the energy required for this process (Saxton and Hollenbeck, 2012). When glutamate is released into the synapse it binds to post-synaptic glutamate receptors on a target neuron. If depolarization reaches its threshold an action potential is generated and propagates along the axon (Vandenberg and Ryan, 2013). When the signal reaches the axon terminal, there is an influx of calcium triggering the release of the neuron's neurotransmitter (Featherstone, 2010; Vandenberg and Ryan, 2013).

There are two main classes of glutamate receptors: ionotropic and metabotropic (Lau and Tymianski, 2010). Ionotropic receptors are directly coupled to ion channels, whereas metabotropic receptors are coupled to G-proteins that mediate intracellular second messenger systems to elicit a response (Lau and Tymianski, 2010). Activation of ionotropic glutamate receptors, including N-methyl-D-aspartate (NMDA), a-amino-3-hydroxyl-5-methyl-4-

isoxazolepropionate (AMPA), and kainate receptors, are the primary mechanism for glutamate excitotoxicity (Molnár, 2018). NMDA receptors play a particularly large role in glutamate excitotoxicity as their activation initiates a large influx of extracellular calcium and sodium into the cell (Molnár, 2018). AMPA and kainate receptors may also contribute to excitotoxicity, although not as drastically because their associated ion channels are at least partially permeable to calcium (Mark et al., 2001).

Under normal physiological conditions, intracellular calcium concentration is maintained at very low levels (~ 100 nM) relative to the extracellular calcium concentrations (2.2-2.6 mM) (Olsen and Sontheimer, 2015). However, overstimulation of glutamate receptors can result in an increase in intracellular calcium levels up to 5 μM-10 μM (Hyrc et al., 1997; Belov Kirdajova et al., 2020). Following tSCI massive amounts of glutamate is released into the extracellular space (Figure 3) when axons are ruptured following impact to the SC (Kaya and Yildiz, 2019; Goldshmit et al., 2020). Surrounding neurons are then subjected to overstimulation from the flood of glutamate creating a cycle of destructive excitatory transmission in the local injury region (Kaya and Yildiz, 2019). The initial glutamate receptor opening of sodium/calcium channels allows for both calcium influx and membrane depolarization (Belov Kirdajova et al., 2020).

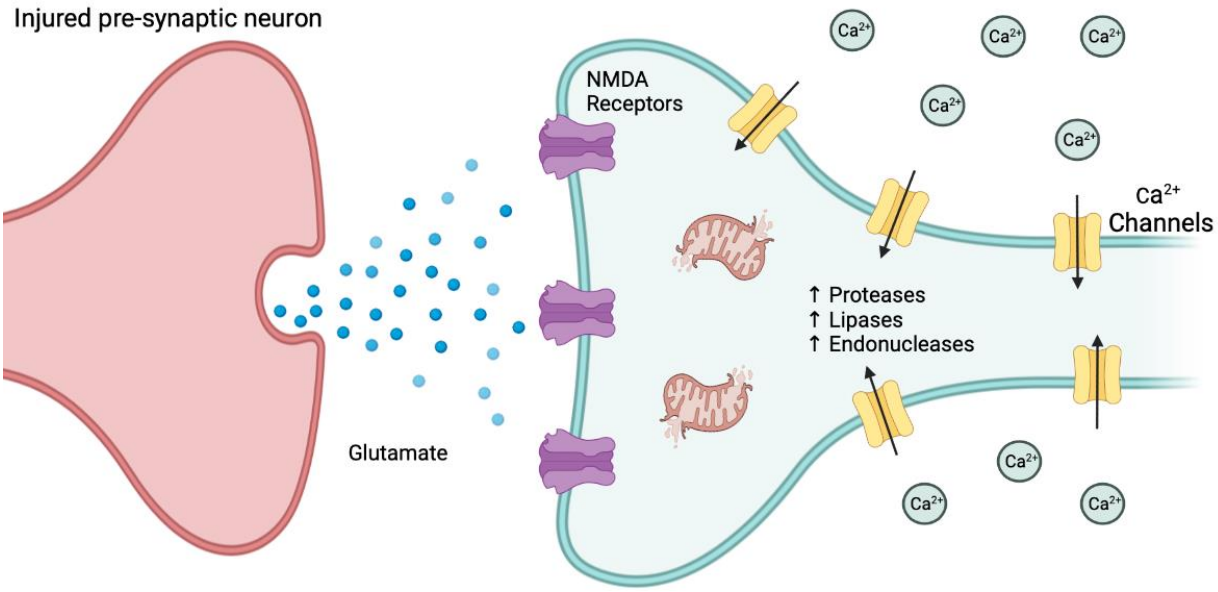

Figure 3: Glutamate excitotoxicity initiated by tSCI. Glutmate from injured axons causes overstimulation of NMDA receptors. Subsequently protease, lipase, and endonuclease activity is increased. Image by Kennedy Brittain using BioRender, 2022.

This decreases the sodium gradient which impedes the ability of the sodium-gradient dependent antiporter to remove calcium (Mark et al., 2001). The high calcium concentration initiates a cascade of deleterious biochemical events that culminate in neurotoxicity and neuronal cell death (Dong et al., 2009). The high calcium levels also trigger a variety of damaging enzymes to become overactivated, namely calpains, caspases, endonucleases, phospholipases, and nitric oxide synthase (NOS), leading to cell death and tissue damage (Kirdajova et al., 2020). Mitochondrial calcium buffering is an evolutionary adaption to mitigate this damage however, their buffering capacity is limited and once overwhelmed, they will collapse and trigger apoptosis.

Under normal physiological conditions, calpains are calcium dependent cysteine proteases located within the cytosol as inactive proenzymes (Pinton et al., 2008). When there is a large increase in intracellular Ca^{2+} they are activated via the autolysis of their N-terminal proteins of both subunits (Pinton et al., 2008). It has been shown that calpains are involved in

mediating the degradation of structural proteins within the nuclear matrix (the cytoskeletal system of the nucleus). The degradation of these proteins triggers apoptosis because they mediate neuronal structural integrity, which is critical for cell survival (Momeni, 2011). When intracellular calcium concentrations are high enough (Figure 4), proapoptotic proteins such as Bcl-2-associated X protein (BAX) and/or Bcl-2 homologous antagonist killer (Bak) are also activated (Elmore, 2007), initiating pore formation on the outer membrane of the mitochondria, leading to the release of a mitochondrial protein called cytochrome C (Zhang et al., 2017). Furthermore, the mitochondrial permeability transition pore (mPTP) contributes to the release of cytochrome C in response to high intracellular calcium concentrations (Elmore, 2007; Zhang et al., 2017). Under normal conditions, cytochrome C is found within the inner mitochondrial membrane (IMM) and participates in the electron transport chain (ETC) by shuttling electrons between complex III and complex IV (Watson and McStay, 2020). However, when cellular homeostasis is disrupted by DNA damage or metabolic stress it is released into the cytosol (Ow et al., 2008). After it is released, cytochrome C binds to a cytosolic protein called apoptotic protease-activating factor-1 (Apaf-1) (Ow et al., 2008). This binding triggers proteins to assemble into a structure known as the apoptosome (Hyun-Eui et al., 2005), which is formed by the conjugation of seven Apaf-1 domains forming the central pore with each domain connected to one cytochrome C (Hyun-Eui et al., 2005). The formation of the apoptosome initiates the

activation of pro-caspase 9 (Bao and Shi, 2007).

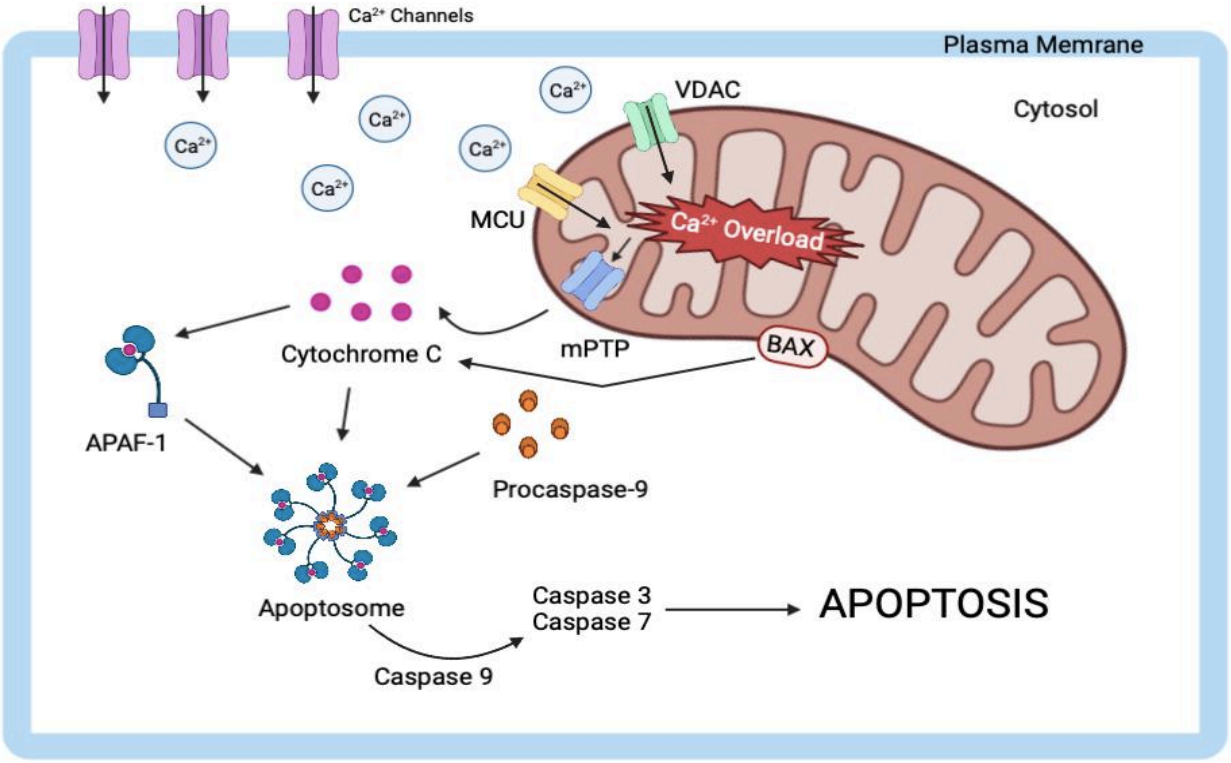

Figure 4: The intrinsic pathway of apoptosis. The intrinsic pathway is activated when cellular homeostasis is disrupted. Proapoptotic proteins such as Bak and/or Bax are activated forming pores in the mitochondrial membrane allowing for the release of cytochrome C. Cytochrome C activates Afap-1 forming the apoptosome which binds and activates caspase-9. Effector caspases are then activated, and apoptosis is triggered. Image created by Kennedy Brittain using BioRender, 2022.

There are two types of caspases that play a role in apoptosis: initiator and effector caspases. Initiator caspases, such as caspase-9, are the first caspases activated by apoptotic signals. The function of these initiator caspases is to activate effector caspases, such as caspase-3 and caspase-7 (Shi, 2004). Caspase-9 achieves this via binding to the central ring of the apoptosome at its N-terminus (Shi, 2004). The Apaf-1 and caspase-9 complex then cleaves and activates caspase-3 and caspase-7 (Bratton and Salvesen, 2010). The activated effector caspases digest proteins and activate DNases thereby mediating the events of apoptosis (Bratton and Salvesen, 2010).

Ischemia and Reperfusion

The spinal cord blood flow is supplied by three primary spinal arteries, one located on the anterior side of the cord and two supplying the posterior portion of the cord (Michael-Titus et al., 2010). These arteries are critical to cell survival in the SC as they deliver oxygen and nutrients (Michael-Titus et al., 2010). However, as these larger vessels often remain intact following SCI, it is failure of the microcirculation, loss of autoregulation, and increases in interstitial pressure that underlie the major disruption of blood flow into the injured region of the SC (Tator and Fehlings, 1991). Between the three major arteries, there are several anastomoses that form a network of blood vessels, referred to as the pial plexus (Miyasaka et al., 2000), which is particularly vulnerable to tSCI given these small anastomoses are highly susceptible to interruptions in blood flow and damage (Mautes et al., 2000). The initial event of primary injury causes physical injury to these blood vessels leading to hemorrhage into the epidural, subdural, subarachnoid, and intramedullary spaces (Mautes et al., 2000).

When the blood supply to the SC is restricted (ischemia) it impedes the delivery of oxygen and glucose to the SC tissues, resulting in hypoxic conditions (Kalogeris et al., 2016). Consequently, cellular respiration within the injured region is hindered and the ATP supply is diminished given the lack of oxygen being delivered to the electron transport chain (ETC). In turn, ionic homeostasis is disrupted due to the failure of the Na^+/K^+ ATPase. This causes a rise in extracellular K^+ concentrations and the opening of non-specific Na^+ channels, depolarizing the neuron (Gourdin, 2013). Depolarization and subsequent Ca^{2+} influx results in further damage due to excitotoxicity (Dong et al., 2009).

Oxidative Stress

Mitochondrial dysfunction is a large contributor to the generation of free radicals due to their role in consuming ~90% of the cell's oxygen (Kausar et al., 2018). Free radicals are highly reactive molecules that possess an unpaired electron in their outer valence shell conferring high chemical reactivity (Kurutas, 2016). Typically, reactive oxygen species (ROS) are found in low levels and are a by-product of oxidative metabolism within the mitochondria (Zorov et al., 2014). However, high levels of these molecules, such as following SCI, can have severely damaging consequences (Zorov et al., 2014). Commonly produced ROS following SCI include superoxide, hydroxyl radical, and hydrogen peroxide (Xu et al., 2005). In addition, iron also generates oxidative stress following SCI (Gupta et al., 2016). The Fenton reaction (Figure 5) occurs when a hydroxide and hydroxyl radical are formed when Fe^{2+} and hydrogen peroxide react (Kehrer, 2000). The Haber-Weiss reaction (Figure 5) is also a product of iron dynamics when a hydroxyl and hydroxide radical are formed when catalyzed by iron (Kehrer, 2000). This is of particular relevance following tSCI because Fe^{2+} enters the mitochondrial calcium uniporter (MCU) with Ca^{2+} during pathological conditions (Uchiyama et al., 2008). The free radicals generated by iron entering through the MCU contribute to mitochondrial degradation and neuronal death via apoptosis (Uchiyama et al., 2008).

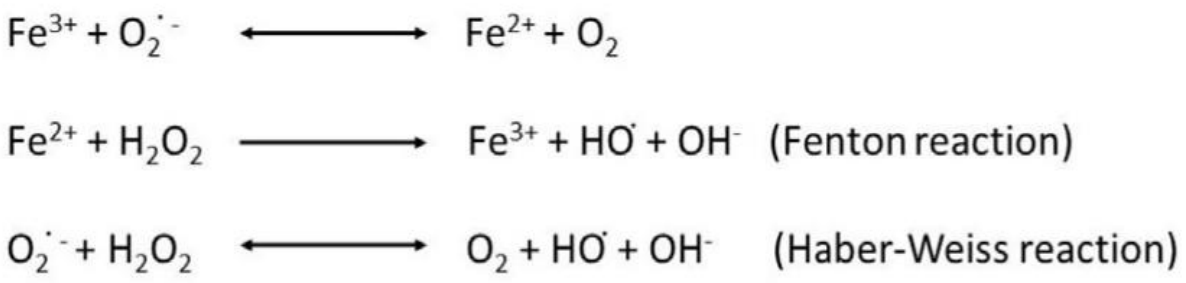

Figure 5*:* The ROS producing Fenton and Haber-Weiss reactions. These reactions are a source of oxidative stress to neurons following SCI (Liu et al., 1999).

ROS can have damaging effects on several cellular components, including proteins, carbohydrates, nucleic acids, and lipids, inhibiting their functions and eventually causing cell death in both neurons and glia (Sbodio et al., 2019). Lipid peroxidation is particularly problematic and occurs when ROS interact with the numerous polyunsaturated fatty acids in the cell membrane. This forms reactive lipids that subsequently form lipid peroxyl radicals (Su et al., 2019). This begins a catastrophic chain reaction with each lipid peroxyl radical reacting with neighbouring fatty acids (Su et al., 2019). The final product of this reaction is 4-hydroxynonenal (HNE) and 2-propenal which are both highly toxic to cells (Su et al., 2019). These products destabilize cellular membranes, and create ionic imbalance, metabolic compromise, and damage to proteins and DNA (Su et al., 2019).

1.5 The Role of Mitochondria in Neuroprotection

Mitochondria play a critical role in cell survival, considering their well-known role in energy metabolism (Gray, 2013). For this reason, it is critical that mitochondrial integrity remain intact following SCI to maximize neuronal survival. Mitochondria contain both an inner and outer membrane that function to strictly regulate the passage of ions in and out of the organelle (Gray, 2013). The outer membrane allows for the passage of ions, ATP, and ADP. The inner membrane, is freely permeable to oxygen, water, and carbon dioxide however, ion passage is tightly regulated (Demirel and Gerbaud, 2019). The electron transport chain (ETC) remains efficient through this tight regulation of ion channels on the inner mitochondrial membrane in order to maintain the electrochemical gradient required for ATP synthesis (Gray, 2013). Reactive oxygen species (ROS) are formed when electrons escaping from the ETC combine with oxygen

in the mitochondrial matrix (Turrens, 2003). Some of these ROS include superoxide anion, hydrogen peroxide, and hydroxyl radicals (Turrens, 2003). Under normal physiological conditions ROS toxicity is prevented by endogenous antioxidants; however, during pathological conditions, such as following a SCI, ATP production is disrupted and there is an increase in ROS to the point beyond antioxidant ability (Zorov et al., 2014). Mitochondrial integrity has been determined to be essential for neuronal homeostasis and survival following SCI (Scholpa and Schnellmann, 2017). Neurons are dependent on efficient ATP production and ion homeostasis to allow for action potential propagation and the uptake/release of neurotransmitters (Scholpa and Schnellmann, 2017).

The critical role mitochondria play in neuroprotection was highlighted in a report by Rawson et al. 2014. Their study employed *C. elegans ric-7* mutants, in which mitochondria are unable to exit the cell body and enter the axon (Rawson et al., 2014). When these mitochondria deficient axons were cut with a laser they rapidly degenerated, some neurons even spontaneously degenerated without injury (Rawson et al., 2014). This degeneration was mediated when mitochondria were forced into the axons of the mutants (Rawson et al., 2014). This effect was also observed in wild-type mice when they observed that axon fragments containing a mitochondrion survived axotomy, whereas those without, degenerated (Rawson et al., 2014).

1.6 The Mitochondrial Calcium Uniporter

Although it has been well-established that mitochondria rapidly take-up calcium across the inner mitochondrial membrane, one of its primary transporters has only recently been discovered: the mitochondrial calcium uniporter (MCU) (De Stefani et al., 2011; Marchi and Pinton, 2014). Mitochondrial calcium balance is required for maintaining cell homeostasis,

which is imperative for cell survival (Mishra et al., 2017). Voltage-dependent anion channels (VDAC's) are the most abundant proteins on the outer mitochondrial membrane (O-Uchi et al., 2014). They are characterized by having a weak anion selectivity in open channel conformation while having strong cation selectivity in closed states (O-Uchi et al., 2014). There are three VDAC isoforms that share similar Ca^{2+} channel affinity ($VDAC_1$, $VDAC_2$, $VDAC_3$). Calcium ions enter the outer mitochondrial membrane through these VDACs and can then be transported across the inner mitochondrial membrane through the MCU during periods of high calcium influx (Mammucari et al., 2017).

The MCU gene is highly conserved in eukaryotes, with the exception of yeasts, and codes for a complex consisting of both pore-forming and regulatory subunits (Jhun et al., 2016). Mitochondrial calcium uptake 1 (MICU1) and mitochondrial calcium uptake 2 (MICU2) proteins are associated with the pore-forming subunit (Figure 6) and act to regulate its activity (Kamer and Mootha, 2015). MICU1 functions as a gate-keeping protein that sets the threshold of calcium required for pore-opening (Mallilankaraman et al., 2012). Whereas, MICU2 is linked to MICU1 and has an inhibitory role in pore opening (Mallilankaraman et al., 2012). It is currently unknown whether MICU2 acts independently from MICU1 to execute its inhibitory role and further studies will be required to clarify their exact mechanisms (Park et al., 2020). Essential MCU regulator (EMRE) is another protein essential for MCU function (Kamer and Mootha, 2015). In mammals it is necessary for uniporter current and helps to mediate the interaction of MICU1 and MICU2 with the pore-forming subunit (Kamer and Mootha, 2015). It is crucial to highlight that the MCU is only activated when local calcium concentrations become higher than ~ 1μM, which occurs during pathological conditions (such as following a tSCI) (Fan et al., 2020).

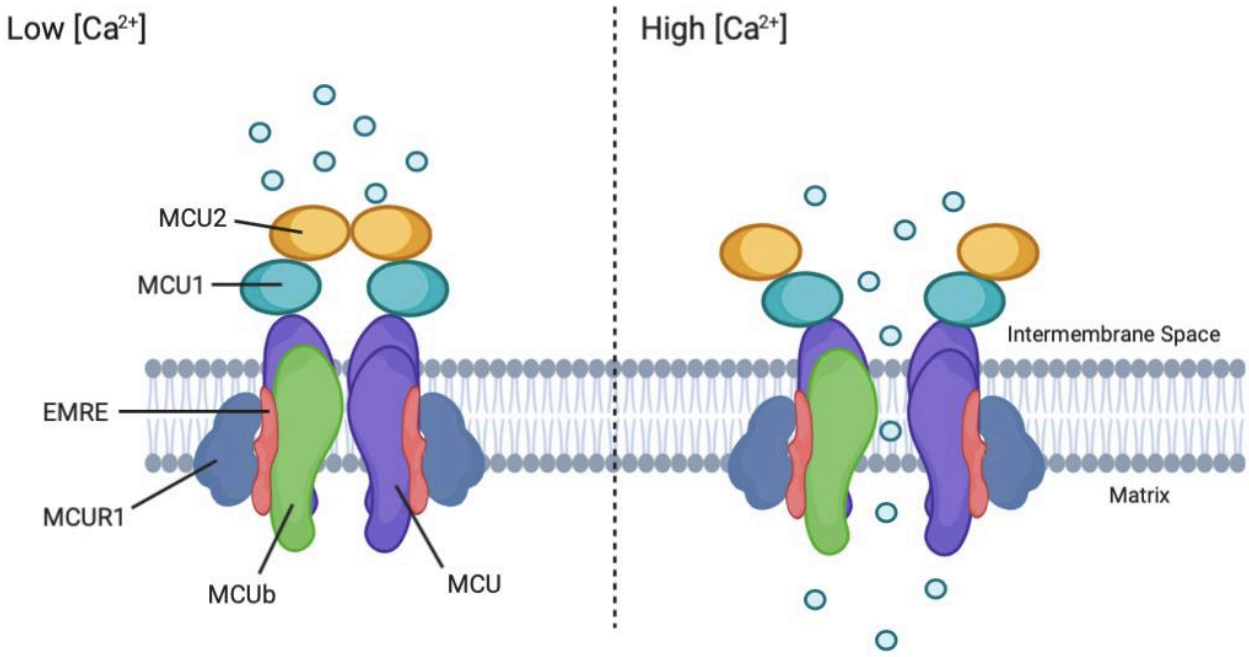

Figure 6: A schematic of the current model of the MCU complex (Mammucari et al., 2016). Image by Kennedy Brittain created using BioRender, 2022.

1.7 Ruthenium 265 and Neuroprotection

Ruthenium-based complexes such as Ruthenium Red and Ru360 have been used as successful inhibitors of the MCU for decades (Moore, 1971; Broekemeier et al., 1994). Ruthenium Red was previously used as a histological stain for glycoproteins and polysaccharides (Fujitsuka and Ito, 1983). While utilizing the compound for histological purposes it was observed that it had channel blocking properties, including inhibition of the MCU (Moore, 1971; Nair et al., 1975). In a traumatic brain injury (TBI) model, blockage of the MCU channel using ruthenium red, prevented iron and calcium overload, increased mitochondrial survival, reduced oxidative stress, increased cell energy supply, and in turn lowered rates of apoptosis (Zhang et al., 2019). Although an effective MCU inhibitor, ruthenium red has undesirable characteristics such as neurotoxicity in addition to a low-yielding and challenging synthesis that make it non-

viable for clinical purposes (Velasco et al., 1995) (Nathan et al., 2017). During commercial preparations of Ruthenium Red, researchers found that preparations of the compound were often less than 20% pure (Ying et al., 1991; Broekemeier et al., 1994). They discovered that the unpurified mixture actually had stronger inhibitory properties than Ruthenium Red and went on to isolate the product and named it Ru360 after its absorbance maxima (Broekemeier et al., 1994; Woods et al., 2020). Although a potent inhibitor, Ru360 had limited therapeutic potential due to its poor cell permeability (Woods et al., 2020). These two inhibitors have been used extensively in the literature for almost 30 years. In 2019, Woods et al. modified Ru360 to create a novel ruthenium-based MCU inhibitor called Ru265 (again named after its absorbance maxima) that is cell-permeable and highly selective for the MCU channel (Woods et al., 2019). Ru265 can be synthesized with moderate yields without strenuous purification processes and was also found to have an improved safety profile (IC_{50}=195 ± 8) μM (Woods et al., 2019). It was also determined that Ru265 was ~11.5 times more effective at inhibiting the MCU, compared to Ru360, due in part to its increased cell-permeability (Woods et al., 2019). Furthermore, Woods et al. tested the protectant ability of Ru265 on cardiomyocytes subjected to a hypoxia/reoxygenation injury. They demonstrated that Ru265 allowed mitochondria to remain viable and that the mitochondrial membrane potential ($\Delta\Psi m$) also remained stable as opposed to untreated cells (Woods et al., 2019).

Ablation of the MCU in cardiomyocytes has been shown to protect mice from ischemia/reperfusion injury further supporting the role the MCU plays in cell survival under stressful physiological conditions (Novorolsky et al., 2020). These promising findings prompted investigations of the protective effects of Ru265 in primary cultures of mouse cortical neurons subjected to oxygen-glucose deprivation (OGD). It was found that with the addition of Ru265

(10 μM) 30 minutes prior to OGD suppressed the generation of calpain-cleaved αII-spectrin 3, a structural protein found in neurons (Novorolsky et al., 2020). In addition, treatment of Ru265 prior to OGD completely preserved mitochondrial respiration and glycolysis 2-hours post injury. Finally, they tested the neuroprotective effects of Ru265 in an adult mouse model of hypoxia/ischemia (HI) brain injury. Relative to saline controls, Ru265-treated mice had reduced sensorimotor deficits and infarct volumes 24 hours following HI (Novorolsky et al., 2020).

1.8 Contusion SCI & Animal Model

There are several different experimental classifications of primary SCI injury that occur. Each class of injury has their own associated aetiologies and pathophysiology (Anjum et al., 2020). Common primary injury types include: impact with continued compression, impact with transient compression, distraction (stretching of the SC), and laceration/transection (Alizadeh et al., 2019). In humans, the most common documented type of primary tSCI is impact with continued compression. For this reason, when using animal models, contusion SCI is of particular interest to researchers because this model perhaps most closely mimics the clinical entity (Alizadeh et al., 2019). The first documented example of an experimental contusion SCI model was performed by Reginald Allen in 1911 when he performed a laminectomy on a canine and dropped a weight onto the exposed SC (Allen, 1911). The contusion model for SCI has since been widely used by researchers in a variety of animal models including primates, felines, and rodents (Young, 2002; Zhang et al., 2014).

Contusion spinal cord injury occurs when the SC receives an impact, which results in compression of the SC at the injury site but leaving the majority of the tissue intact (Ju et al., 2014). These injuries are characterized by a core of necrotic tissue surrounded by a rim of

demyelinated axons (Ju et al., 2014). Contusion devices are often used to deliver acute injuries to the spinal cord. Critical factors to consider when using contusion models include height, dwell-time, force, displacement, and velocity upon impact to the SC (Cheriyan et al., 2014). There are currently three primary types of contusion animal models, namely weight-drop apparatus, electromagnetic impactor, and an air gun device (Cheriyan et al., 2014).

Mouse models are becoming increasingly popular for studying SCI (Lilley et al., 2020). Although larger mammals better approximate human anatomy and physiology, they are rarely used due to ethical considerations and husbandry constraints (Sharif-Alhoseini et al., 2017). Mice, however, are cost-effective models that have a very well understood anatomy, ease of handling, and a short reproductive cycle (Lilley et al., 2020). In addition, there are numerous transgenic lines of mice available that allow researchers to address specific questions involving gene function and modelling of human disease (National Research Council, 1994). They are excellent models for studying basic cellular and molecular biology following spinal cord injury as many of the pathological processes mimic those of humans (Sharif-Alhoseini et al., 2017).

1.9 Study Objectives

Mitochondria play an essential role in neuronal survival following tSCI. Early rescue of mitochondria using mitoprotective compounds may alleviate numerous sequelae of SCI. As reviewed above, several secondary injury cascades are initiated and connected by mitochondrial damage or death. Previous studies have demonstrated that without properly functioning mitochondria, neurons subjected to injury are unable to repair themselves, and in turn undergo apoptosis. Inhibition of the MCU located on the IMM has previously shown promising neuroprotective effects; however, the earlier compounds used have undesirable characteristics and low efficacy. For this reason**, the overarching goal of this research is to use the novel**

ruthenium based MCU inhibitor, Ru265, following tSCI to investigate its potential mitoprotective and neuroprotective properties. This was accomplished through a series of experiments with the following aims:

Aim 1) Determine if Ru265 crosses the spinal meninges when applied to the dura following tSCI.

During early studies and model establishment, it was observed that following administration of Ru265 mice exhibited seizure-like behaviours. This prompted us to investigate localized methods of drug delivery prior to evaluating Ru265's potential mitoprotection and/or neuroprotective effects. The effectiveness of intraperitoneal (IP) injection and epidural delivery of Ru265 were assessed and compared.

Aim 2) Determine the mitoprotective effects of Ru265 following tSCI.

The proposed mechanism of action of Ru265 is to inhibit the MCU, therefore preserving mitochondrial function and integrity. To evaluate if Ru265 improves mitochondrial survival following tSCI, electron microscopy was performed 4 hours post-injury to evaluate structural integrity.

Aim 3) Determine the neuroprotective effects of Ru265 following tSCI.

Mitochondrial integrity is critical for neuronal survival following tSCI. For this reason, if Ru265 improves mitochondrial integrity it is predicted that this will translate into neuroprotection following injury. To evaluate neuronal survival fluorescence microscopy was performed 72 hours post-injury on SCI tissue section to visualize labelling by a neurodegeneration marker.

2.0 LOCAL DELIVERY OF RU265 BY EPIDURAL APPLICATION FOLLOWING TRAUMATIC SPINAL CORD INJURY: OPTIMIZATION AND EFFICACY

2.1 Introduction

While establishing our SCI model, seizure-like behaviours were observed following delivery of Ru265 via intraperitoneal (IP) injection, at doses similar to those previously reported (Novorolsky et al., 2020). These behaviours ranged from mild to severe and included one or more of whisker trembling, motionless staring, facial jerking, and tremors. This resulted in mice being sacrificed before the planned experimental end date due to *a priori* animal humane endpoints. Systemic administration of the drug likely suppressed MCU across all regions, *including* uninjured CNS tissue where it was not desirable. This also required greater total amounts of drug being delivered to achieve effective concentrations in and around the injured SC tissue. These considerations prompted us to investigate localized methods of drug delivery to mitigate some of the undesirable systemic effects of the drug.

By delivering the drug locally, directly upon or close to the lesion site, the total mass of drug used could be lowered greatly whilst achieving effective local tissue concentrations faster. After careful consideration, epidural delivery was the mode chosen. Epidural application involves directly placing a dose of Ru265 onto the exposed dura mater following a laminectomy (removal of the lamina) and tSCI. This mode of delivery was chosen as it has shown to be promising in pre-clinical studies and an ongoing clinical trial, where a drug called Cethrin (a Rho inhibitor which is proposed to promote neuronal regrowth) is applied epidurally (Vertex Pharmaceuticals Incorporated, 2007). The early phases of this trial have reported that epidural delivery of Cethrin appears promising with improvements in motor scores (Fehlings et al., 2011; McKerracher and Anderson, 2013).

This mode of delivery is provocative for clinical treatment as the dura mater is routinely exposed within the first 24 hours of injury during surgical intervention for decompression and/or stabilization of vertebral fractures (Ramakonar and Fehlings, 2021). Furthermore, in our SCI model the lamina is surgically removed to expose the spinal cord prior to delivering the impact, making this method of drug delivery feasible and efficient.

2.2 Methods

2.2.1 Animals

Female transgenic mice (*Mus musculus,* common house mouse) of the strain Thy1-YFP B6.Tg.Cg. 16Jrs/J of C57BL/6J background was chosen as the model species for all experiments in this study. This strain expresses YFP at high levels in motor and sensory neurons allowing for visualization of labelled axons. Spinal cord injury often disrupts urinary bladder function, requiring full bladders to be manually expressed in mice at least 3 times every day until such function is regained after 1-2 weeks. Bladder expression is much easier in female mice, reducing the risk of complications such as bladder rupture or urethral blockage during recovery (Lilley et al., 2020). Breeder mice were originally obtained from The Jackson Laboratory (www.jax.org) and bred at the Dalhousie University animal care facilities. Only young adult mice between the ages of 12-16 weeks were used. This age is particularly relevant because most tSCI's in humans occur in young adults (Thomas and Grumbles, 2014). All animal procedures were performed in accordance with Dalhousie University's Animal Care and Use Committee (Protocol #20-011).

2.2.2 Experimental Spinal Cord Injury

The weight of each mouse was recorded prior to surgery. Injury impact was delivered via an Infinite Horizon Impactor (IH-0400, Precision Systems & Instrumentation, Fairfax VA,

USA). Control software (Neural PSI IH Spinal Impactor v5.0) allowed standardization of the force at 50 kD and dwell time to 0 sec. A force of 50 kD has been classified as a moderate injury (compared to mild (30 kD) and severe (70 kD) injuries) (Nishi et al., 2007). Moderate injuries provide an impact to the SC sufficient to provide visible motor deficits (hind-limb paralysis) and notable cell death (Lee et al., 2012). This allows for therapeutic effects to be discernible, but not so severe that animal welfare would be severely reduced (including mortality) (Lee et al., 2012). These parameters were tested on artificial testing material of consistency comparable to spinal cord tissue three times to ensure all equipment was functioning as expected before proceeding with experimental surgery and impact (Figure 7). Injury parameters were between control and treatment animals were determined to be consistent by plotting force and displacement values (Appendix, Figure 23). The surgical area was sterilized prior to anaesthesia, using H_2O_2 spray. Following induction of general anaesthesia (oxygen 1 L/min; isoflurane 4%), the mouse was prepped and placed on a heated surgical platform, and isoflurane turned down to 1.5% and maintained for the duration of the procedure. Buprenorphine Sustained-Release (Bup SR) (0.05 mg/kg), was injected subcutaneously in the neck region. Lacrilube (Refresh®), a sterile lubricating eye ointment was applied onto both eyes for the duration of the procedure. After checking for absence of hind-paw pinch reflex, the skin was incised rostral-caudally for approximately 1 cm centered over the T10 lamina. Muscle layers were carefully reflected to expose the vertebrae T9, T10, and T11. Lamina T10 was then carefully removed using ronguers exposing the T12 spinal segment and the vertebral column was stabilized by clamping with gripping forceps attached to the end of ball-joint arms on the impactor stage. The entire stage and mouse were then moved to the impactor. The impactor head was positioned at a distance of ~4-5 mm directly above midline of the exposed spinal cord. An impact was delivered and confirmed

by noting the hind limb jerk reflex on contact. The stage and mouse were then moved back to the surgery station and following delivery of the drug or vehicle, the muscle and skin layers were sutured. The animal was then brought to the recovery area and monitored with due post-surgery care until euthanasia at predetermined experimental endpoints.

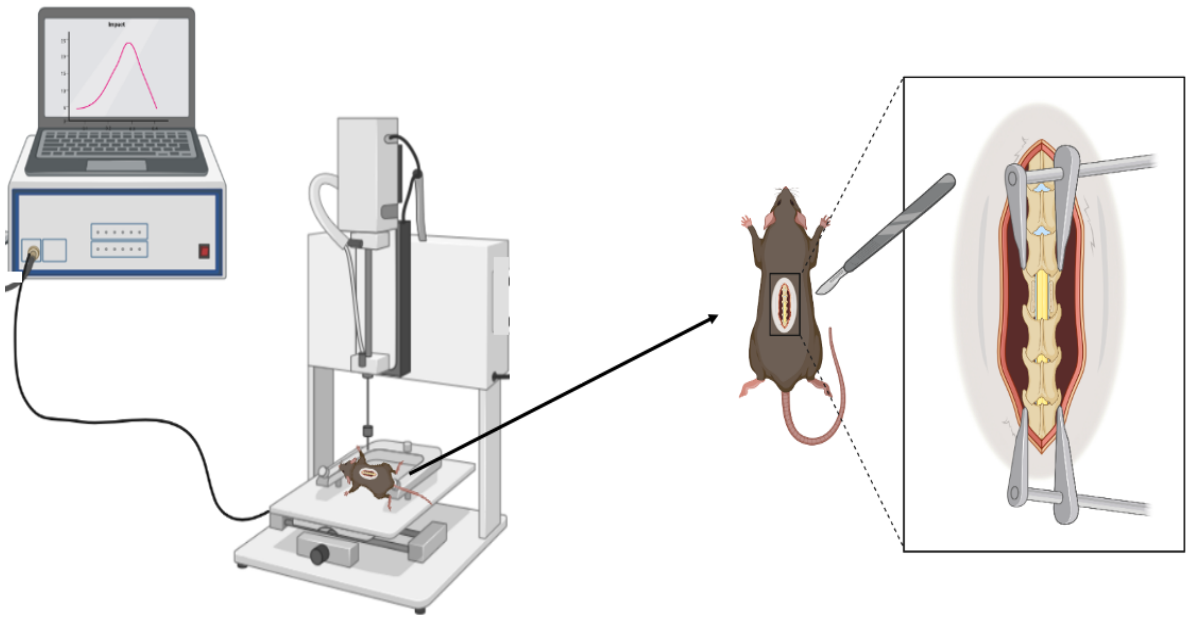

Figure 7: Experimental set-up for delivery of a tSCI. Image creating by Kennedy Brittain using BioRender, 2022.

2.2.3 Dose Determination & Epidural Delivery

Prior to delivery of Ru265 epidurally, it was critical to optimize the dose to be applied. The maximally tolerated dose was considered to be the amount of Ru265 that could be delivered without yielding observable seizure-like behaviours. To do this, we first assumed that the previously reported IP dose (0.0625 mg) may be too low considering it would have to travel through all three meningeal layers when applied to the dura mater. Considering this, the first dose utilized was 0.1875 mg (3X the previously reported IP dose), however, the mice exhibited intense seizure-like behaviours. We titrated down the dose from 3X, 1X, and 0.5X the previously

reported IP dose. In all these instances the mice still exhibited some seizure-like behaviours in roughly dose dependent severity. Finally, at 0.4X the original dose the animals convalesced well and no seizure-like behaviours were observed. As such, 0.025 mg was determined to be the maximally tolerated dose and was used when delivering Ru265 in following experiments. To deliver Ru265 epidurally (Figure 8), a 50 mM suspension of Ru265 in PBS was prepared and following laminectomy and tSCI, a 2 µL micropipette was used to deliver 0.91 µL of the 50 mM solution (0.025 mg Ru265) considering the mice are each of approximately 25 g body weight. For IP injection groups 2 mice were sampled for each time point (4, 8, and 24 h post-injury), and 4 mice were sampled at each time point in the epidural delivery groups (more mice were sampled in this group based on the assumption of increased variability using this method of drug delivery).

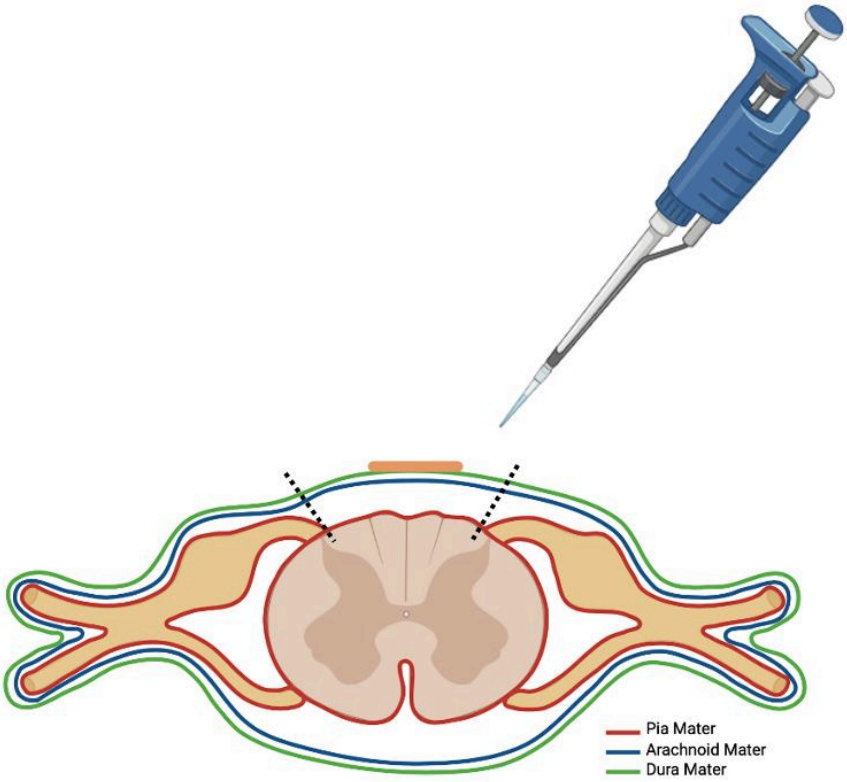

Figure 8: A schematic of epidural drug delivery to the SC. The drug is measured using a pipet and applied directly onto the dura mater following a laminectomy and tSCI. Black dotted lines represent the approximate location of laminectomy and spinal cord exposure with an epidural bolus of Ru265 delivered. Image created by Kennedy Brittain using BioRender, 2022.

2.2.4 Tissue Collection

Mice were euthanized (4, 8, and 24 h post-injury) using an overdose of Euthansol® (340 mg/mL sodium pentobarbital) at a dose of 250 mg/kg IP. Before proceeding, absence of the hind-paw pinch reflex was confirmed. Whole blood was extracted from mice via live cardiac puncture. The heart was exposed by lifting the sternum and any tissue surrounding the heart was trimmed away. A 22 gauge needle on a 1 mL syringe flushed with sodium citrate to prevent coagulation was then carefully inserted into the apex of the heart and 300 µl blood was drawn, transferred into a microcentrifuge tube and stored at -20°C until freeze-drying. The mice were then transcardially perfused with approximately 5 mL of PBS. Approximately 5 mL of PBS was carefully pushed into the left ventricle until the animal was exsanguinated. The spinal column was isolated from the cervical to upper lumbar region and trimmed until the SC was visible at both ends. Hydro-dissection with an 18 gauge edge blunted needle on a 10 ml syringe containing PBS extracted the entire SC in one specimen. Once isolated, 1 cm of the SC was cut centered on the visible lesion site. The SC tissue was carefully placed into a 2 mL microcentrifuge tube, weighed, and stored at -20 °C until freeze-drying. To isolate the forebrain, mice were decapitated, and the skull was bisected by cutting in an upward motion along the sagittal suture beginning at the brain stem. The brain was removed and placed into a petri dish with PBS. For mass spectrometry (MS) analysis it was determined that a standardized portion of the forebrain would be removed. The forebrain was chosen due to the sufficient blood flow in this region which would be relevant for determining if Ru265 was reaching the brain by systemic circulation. After removing the olfactory bulbs, a cut was made 2 mm from the rostral-most portion of the forebrain and was then placed into a microcentrifuge tube and stored at -20°C freezer until freeze-drying.

2.2.5 Inductively Coupled Plasma Mass Spectrometry (ICP-MS) Sample Preparation

Mass Spectrometry protocols and analysis were performed by the Health and Environment Research Centre (HERC) Lab. Quartz digestion vessels were soaked in 10% (v/v) hydrochloric acid (HCl) bath overnight to remove any trace metals and rinsed three times with deionized water. Freeze-dried mouse brain and spinal cord samples were weighed with a microbalance (Sartorius Pinnacle Series model YDS01PI, Denver Instruments) calibrated using 1 mg to 100 mg calibration weights. After weighing, the freeze-dried forebrain and spinal cord samples were placed into the digestion vessels, and 300 µL Type-I deionized water, 500 µL trace metal grade hydrogen peroxide, and 200 µL trace metal grade concentrated nitric acid were added to each vessel. The samples were capped, and microwave digested (CEM model SP-D) at 185°C and 100 psi for 5 minutes. Solid samples require digestion to be converted to ionic form prior to entering the mass spectrometer in order to be detected. After digestion, 9 mL of deionized Type-I water was added and the samples were transferred to 15 mL polypropylene conical tubes. Lastly, the samples were filtered through 0.45 µm cellulose acetate filters (VWR P/N 75846-842). Three method blanks were prepared alongside freeze-dried mouse brain and spinal cord samples. A 200 µL volume of mouse whole blood was added to a digestion vessel, then 700 µL deionized Type-I water, 100 µL trace metal grade hydrogen peroxide, and 200 µL trace metal grade concentrated nitric acid were added to each vessel. Vessels were capped and blood samples were microwave digested at 185°C and 100 psi for 5 minutes. After digestion, 9 mL of deionized Type-I water was added to each sample and samples were transferred to 15 mL polypropylene tubes. Three method blanks were prepared alongside mouse whole blood samples. Samples were vortexed immediately before ICP-MS analysis to ensure homogeneity.

2.2.6 ICP-MS Analysis

The concentration of ruthenium (Ru) in mouse brain, spinal cord, and whole blood samples was measured using an inductively coupled plasma mass spectrometer (ICP-MS, iCAP Q, Thermo Scientific, MA USA) outfitted with a quartz torch, PFA nebulizer, and quartz spray chamber. The torch position, nebulizer flow rate, and lens voltages were tuned daily according to the instructions of the manufacturer using a multi-element tuning solution (P/N THERMO-4AREV-500M, Inorganic Ventures, VA USA). The sample introduction system consisted of an ESI SC-4 DX autosampler and FAST valve (Elemental Scientific, NE USA) to facilitate on-line addition of a 10 µg/L indium internal standard in 2% (v/v) nitric acid (Fisher Scientific, ON Canada). Once samples enter the MS, the high temperature plasma produces ions from the sample which are sorted by their mass-to-charge (m/z) ratios. A quadrupole is used to filter ions from neutral atoms and photons. Ions are then counted with a channel electron multiplier. Measurements were performed in kinetic energy discrimination (KED) mode using high purity He (>99.999%) as the collision gas. In KED mode, the inert He ions will collide with themselves more frequently than with the analyte (Ru). Collisions cause a reduction in the amount of kinetic energy possessed by that ion. An energy barrier is in place following these collisions to that only the higher-energy Ru ions are able to pass through, reducing background signals. A stock Ru standard (Inorganic Ventures, VA USA) was diluted to 0.01, 0.05, 0.1, 0.5, 1, 5, and 10 µg/L in 2% (v/v) nitric acid to form a seven-point calibration curve encompassing the expected analyte concentrations. A quality control check standard (1 µg/L Ru) and blank were measured every 10 samples. Each sample was injected once and measured ten times. Qtegra Intelligent Scientific Data Solution software (version 2.10, Thermo Scientific, MA USA) was used to collect and

process data from ICP-MS analysis. Using a least-squares regression line (y=mx+b) Ru concentrations were calculated.

2.3 Results

Mass spectrometry (MS) revealed an increase in the concentration of Ru within the SC when Ru265 was applied epidurally compared to IP injection. Following epidural application, as time progressed from 4 to 24 hours post-injury there was an accompanying increase in the concentration of Ru265 penetrating the SC. The Ru265 levels within the spinal parenchyma notably increased from 4 to 8 hours (0.54 μM to 0.87 μM) and had a smaller increase from 8 to 24 hours (0.87 μM to 1.01 μM). However, when delivered by IP injection the Ru265 concentrations stayed nearly the same from 4 to 8 hours (0.09 μM to 0.08 μM) and decreased after 24 hours (0.04 μM). For all three time points there was substantially more Ru265 within the spinal cord after epidural application compared to IP injection. From 4, 8 to 24 hours there was 4.5X, 10.9 X, and 25X more Ru265 in the spinal after epidural application to IP injection, respectively (Figure 9).

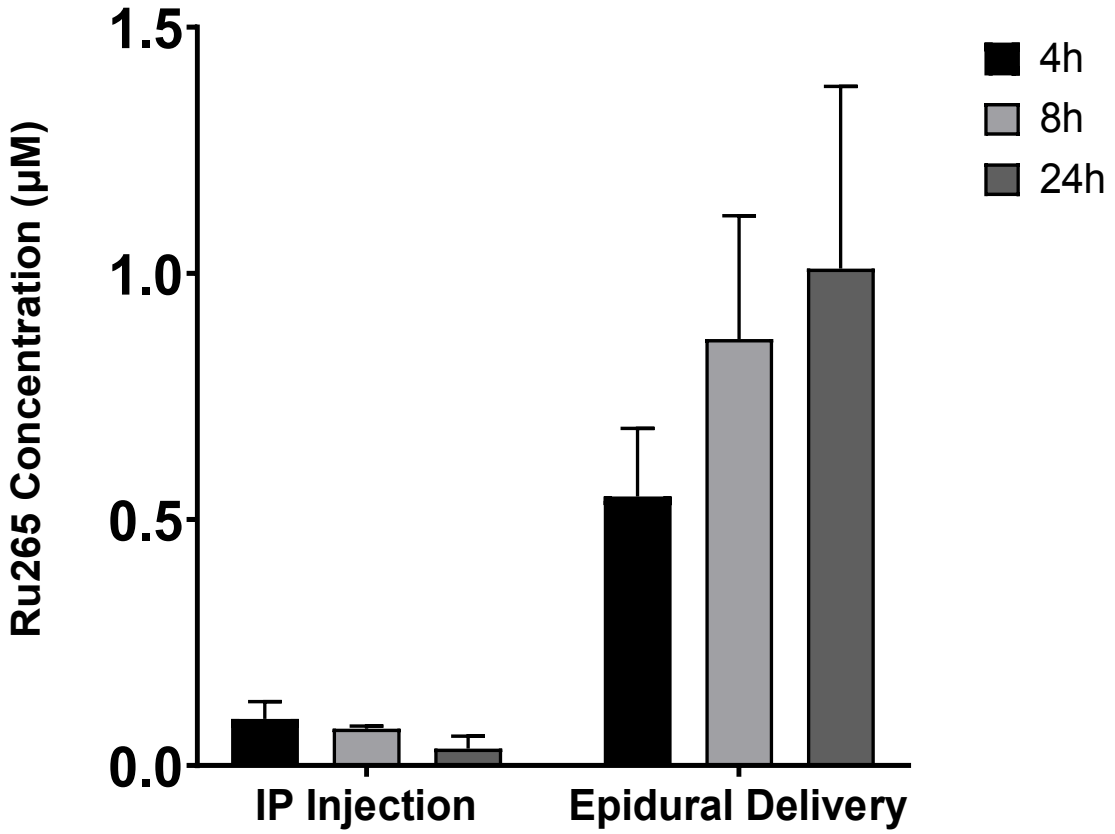

Figure 9: Ru265 concentrations in the spinal cord parenchyma following intraperitoneal and epidural delivery. Bars represent the mean ± SEM.

MS data revealed that the concentrations of Ru265 found in the forebrain following epidural application and IP injection were very similar. There were also no changes in Ru265 concentrations as time post-injury increased from 4 to 24 hours. Interestingly, for both modes of delivery the concentrations were the same at 4 (0.23 μM ED, 0.20 μM IP), and 24 hours with a 0.01 μM decrease at the 8-hour time point (Figure 10).

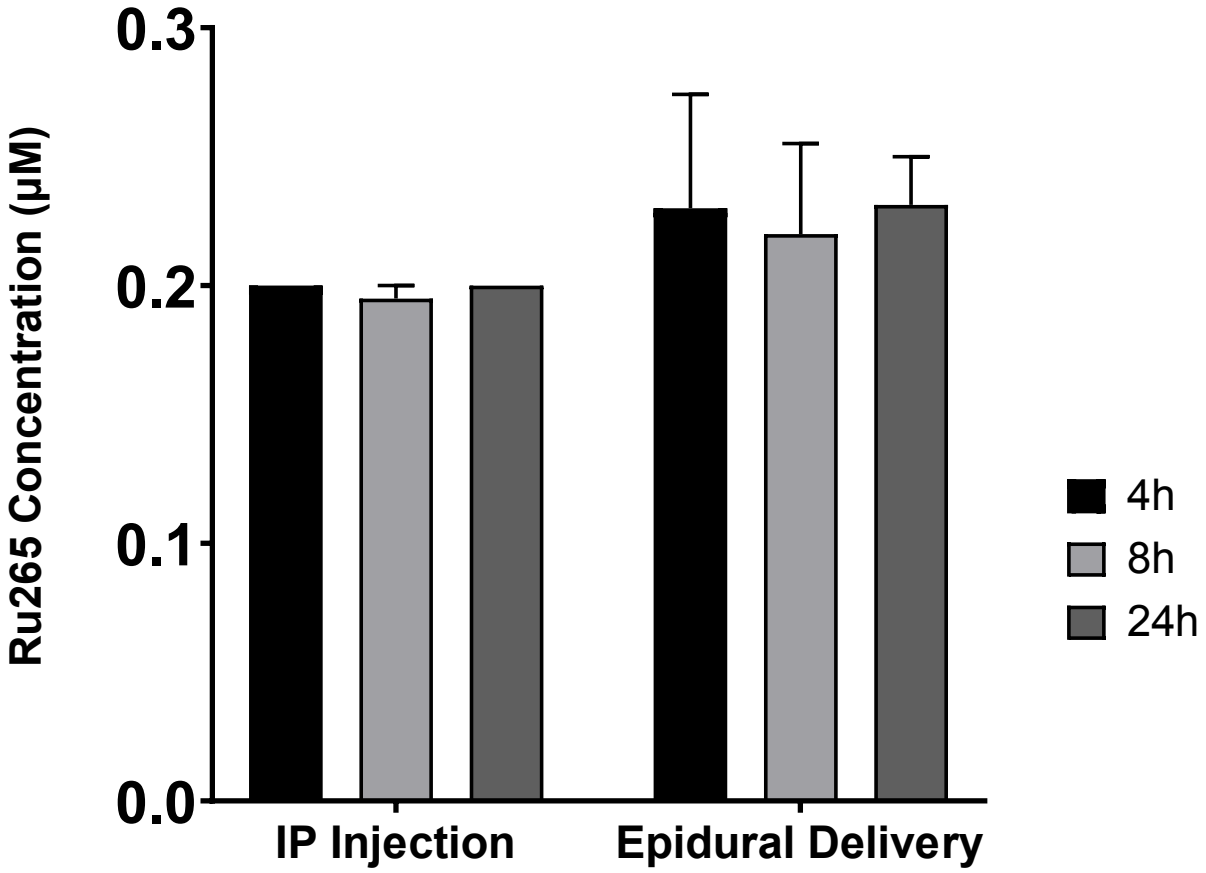

Figure 10: Ru265 concentrations in the forebrain following tSCI delivered epidurally and by IP injection 4-, 8-, and 24-hours post-injury. Bars represent the mean ± SEM.

Whole blood Ru265 concentrations demonstrated an increase of Ru265 following IP injection when compared to epidural application, apart from 24 hours following IP injection. Considering the concentrations achieved following epidural application over time, the values remained relatively stable with a slight decrease from 40 nM to 31 nM from 8 to 24 hours post-injury. However, in the animals where the drug was delivered by IP injection there was a notable decrease in Ru265 levels 24 hours post-injury (to ~0.5X the concentrations at 4 and 8 hours) (Figure 11).

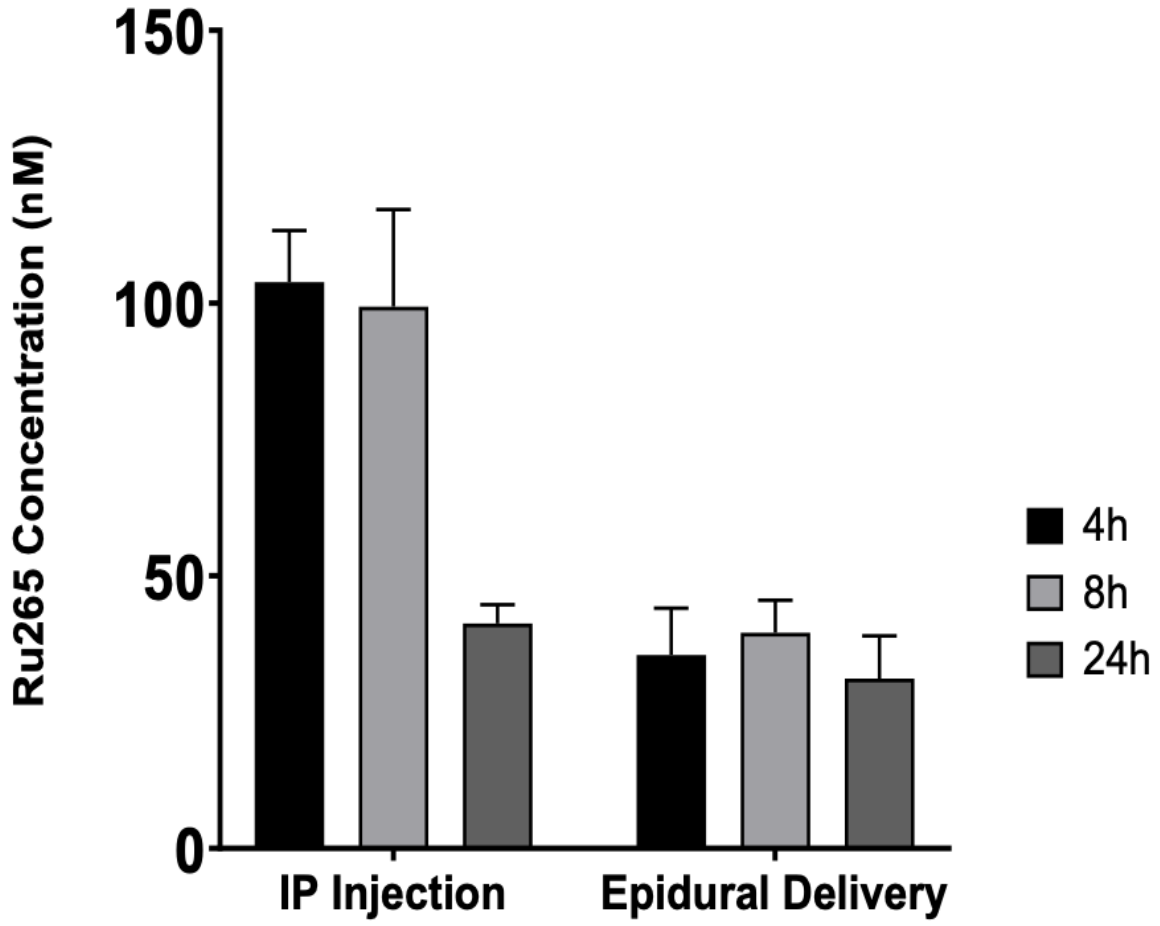

***Figure 11**:* Ru265 concentrations from whole blood following tSCI delivered epidurally and by IP injection 4-, 8-, and 24-hours post-injury. Bars represent the mean ± SEM.

Figure 12 provides a comparison of all three sample types (blood, brain, and SC) at each time point. Compared to other methods it is evident that epidural application of Ru265 penetrates the SC notably more. The previous reported effective Ru265 concentration lies between the red lines on Figure 12 (0.026 µM-0.315 µM) (Novorolsky et al., 2020). Even at 4 hours post-injury the Ru265 concentrations were found to be well above this range (0.54 µM).

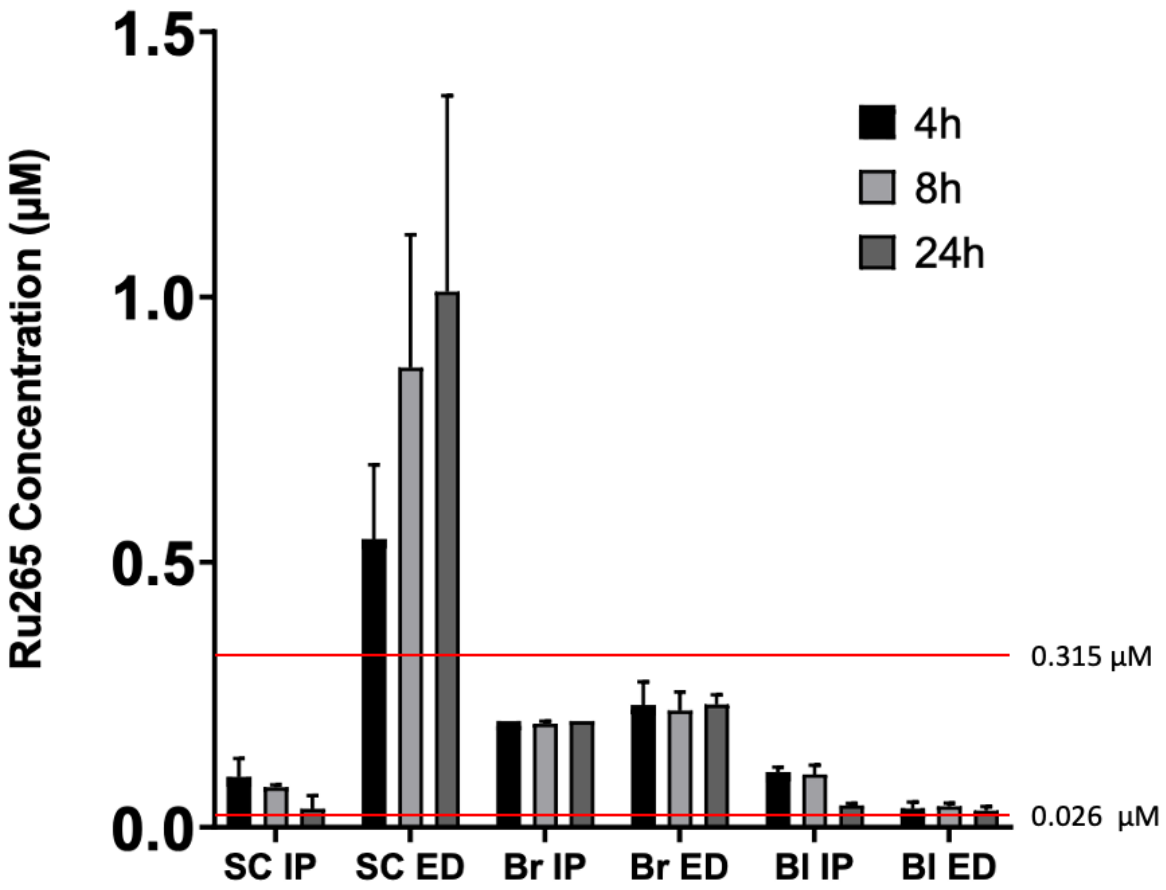

***Figure 12**:* Combined graph of Ru265 concentrations from spinal cord (SC), brain (Br), and whole blood (Bl) following tSCI delivered epidurally and by IP injection 4-, 8-, and 24-hours post-injury. Bars represent the mean ± SEM. Red lines on graph indicate range of effective concentrations (0.026 µM-0.315 µM) based on Novorolsky et al. 2020.

2.4 Discussion

There is considerable increase in the concentration of Ru265 penetrating the spinal cord parenchyma when applied epidurally compared to IP injection. In a previous study, Ru265 was delivered by IP injection and similar to our observations they saw pro-convulsant effects when giving the drug (Novorolsky et al., 2020). Their maximally tolerated dose was determined at 3 mg/kg due to lack of severe seizure behaviours (mild to severe clonic seizures, whisker trembling, etc.). They performed mass spectrometry within the forebrain after delivering 1 mg/kg and 10 mg/kg of Ru265 by IP injection, forebrain concentrations of Ru265 were 0.026 μM and 0.315 μM, respectively. Novorolsky et al. 2020 found significant improvements at 3 mg/kg, we can assume that the effective concentration of the drug lies between their MS concentrations detected at 1 and 10 mg/kg IP. Considering the MS concentrations in our study following epidural application, even at the lowest concentration 4 hours post-injury the Ru265 concentration is 0.54 μM, which is well above the effective dose based on previous work (Novorolsky et al., 2020). Although statistical analyses were not performed due to the small sample sizes used, the objective of this study was met considering we were able to determine that Ru265 does cross the spinal meninges in amounts that are effective to elicit drug effects. In addition, due to Ru265 being a suspension and not a true solution at 50 mM, it has very low viscosity and because of this when placing onto the SC dura would sometimes flow out of the direct region of impact. Future studies should consider better formulations of the drug that are more viscous and more likely to confine the drug to the delivery site. Regardless, these findings suggest that epidural application is a promising method of localized drug delivery following tSCI.

Similar concentrations of Ru265 being observed in the forebrain following epidural delivery and IP injection could be explained by a few possibilities. Firstly, it is well established that IP injection of pharmaceuticals in mice enters the systemic circulation and lymphatic system very rapidly (within 10 seconds) where it is being carried to the brain (Al Shoyaib et al., 2019). However, how it gets to the brain following epidural application is not as easily elucidated. Following a tSCI, there is often blood-vessel rupture that occurs at the impact site (Mautes et al., 2000). Mechanical trauma to the cord damages the microcirculation and disrupts the integrity of the blood-spinal cord barrier (BSCB) causing an increase in its permeability (Whetstone et al., 2003). The increased permeability persists from 3-7 days post-injury before it is able to repair itself (Whetstone et al., 2003). One possible explanation is that when applying the drug epidurally it can enter the blood stream due to blood vessel rupture and increased BSCB (likely to a lesser extent) permeability allowing it to reach the brain through the circulation in similar concentrations to those achieved with IP injection.

Another possible avenue of Ru265 getting to the brain is that when diffusing through the meningeal layers, Ru265 is entering the CSF within the central canal and travelling to the brain as it circles back to the ventricles. In a previous study, transdermal administration was used as a novel method for brain-targeted drug delivery (Lehrer and Rheinstein, 2019). This study aimed to find a more localized method of drug delivery for delivering non-steroidal anti-inflammatory drugs (NSAIDs) in the treatment of Alzheimer's disease (AD) (Lehrer and Rheinstein, 2019). In this method cervical spinal transdermal patches were applied, and the drug diffused through the intervertebral space, penetrated the dura mater, and entered the CSF, where it is was carried to the brain (Sun et al., 2021). Although applied to the skin, this method is similar to epidural

application in the pathway that it takes to elicit its effects and therefore provides support that its possible Ru265 may be entering the CSF and travelling to the brain.

Lower concentrations of Ru265 observed in the blood following epidural application supports that this is a promising method of localized drug delivery. Less Ru265 in circulation helps to prevent undesirable side-effects in non-injury regions of the body where its effects are not required. The significant decrease observed at 24 hours is likely due to Ru265 being renally excreted (Ruthenium Red, MSDS, CHEMWATCH 2010).

3.0 AN INVESTIGATION OF THE MITOPROTECTIVE AND NEUROPROTECTIVE PROPERTIES OF RU265 FOLLOWING tSCI

3.1 Introduction

With epidural delivery established as an effective mode of delivery for Ru265, an investigation of the drug's potential mitoprotective and neuroprotective effects followed. To determine if Ru265 had mitoprotective properties transmission electron microscopy (TEM) was performed in order to evaluate structural integrity of mitochondria in control and Ru265 treated specimens. TEM is a valuable tool for measuring morphological differences in mitochondria (Sasaki, 2010). The organelles themselves are of interest due to their heterogeneity that reflects the physiological status of cells (Sasaki, 2010). Intact cristae morphology is critical for oxidative phosphorylation and therefore ATP production (Jia et al., 2016). Loss of ATP has been documented to occur following tSCI contributing to death of mitochondria and in turn neurons (Jia et al., 2016). TEM allows for determination of whether Ru265 treatment maintains mitochondrial integrity, by allowing visualization of cristae and mitochondrial membranes.

Neuronal survival can be evaluated through Fluoro-Jade C (FJC) labelling. Fluoro-Jade staining has become a popular tool for labelling degenerating neurons, regardless of the manner of cell death including apoptotic, necrotic and autophagic (Ikenari et al., 2020). It is an anionic fluorochrome that is comparably selective yet much simpler than other methods used for labelling neuronal degeneration (Schmued et al., 1997). It stains degenerating cell bodies, dendrites, axons and axon terminals bright green (excitation: 485 nm, emission: 520 nm) making the structures easily identifiable (Schmued et al., 2005). Interestingly, the mechanism by which Fluoro-Jade stains degenerating neurons remains unknown (Schmued et al., 2005). Following the original identification of Fluoro-Jade, Fluoro-Jade B and Fluoro-Jade C were more recently developed. These optimized stains provide an even higher intensity and specificity for degenerating neurons compared to Fluoro-Jade due to the addition of a sulfite ester (previously

was a sulfonate group) (Schmued et al., 2005). FJC staining can also be combined with Hoechst to label nuclei (excitation: 350 nm, emission: 461) in all living cells, and NeuN immunolabelling (Chazotte, 2011). NeuN, also known as Fox-3, is a neuronal nuclear antigen which specifically labels neuronal nuclei (Kim et al., 2009). These immunohistochemical techniques allow for the determination of the potential neuroprotective effects of Ru265 by quantification of the number of FJC positive neurons in control and treated specimens.

3.2 Methods

3.2.1 Electron Microscopy Sample Preparation

Four mice (Thy1-YFP B6.Tg.Cg. 16Jrs/J of C57BL/6J background) from each control (received PBS epidurally) and treatment (received Ru265 epidurally) groups were sacrificed 4 hours post-injury to evaluate mitochondrial integrity. The 4-hour time point was chosen based on previous studies that established altered mitochondrial morphology following SCI begins as early as 2 hours (organelles become larger/swollen) and is well established by 4 hours post-injury (swollen with disordered cristae) (Jia et al., 2016). All mice received a tSCI using the previously described model and were given either PBS or Ru265 epidurally at the same volume of 0.94 μL (0.025 mg). Mice were euthanized as previously described and the spinal cord of each mouse was isolated by performing a serial laminectomy (dissecting the spinal vertebrae one at a time) and placed into 4% PFA in PBS overnight. The following day the SCs were placed in 15% sucrose for 24 hours and then in 30% sucrose until further processing.

3.2.2 Transmission Electron Microscopy

Samples were fixed for 2 hours (minimum) with 2.5% EM grade glutaraldehyde (Electron Microscopy Sciences, #16210) diluted with 0.1M sodium cacodylate buffer. They were

then rinsed 3 times (10 minutes minimum each) with 0.1M sodium cacodylate buffer and subsequently fixed with 1% osmium tetroxide for 2 hours. Samples were rinsed with distilled water and stored overnight at 4°C in 0.25% uranyl acetate. SC samples were then dehydrated with a graduated series of acetone: 50% acetone 10 minutes, 70% acetone 10 minutes X2, 95% acetone 10 minutes X2, 100% acetone 10 minutes X2. Epon Araldite resin was then used to infiltrate samples at a:

3:1 ratio … 3 parts dried 100% acetone : 1 part resin for 3 hours

1:3 ratio … 1 part dried 100% acetone : 3 parts resin overnight

100% Epon Araldite resin for 2 x 3 hours

Samples were next embedded in 100% Epon Araldite Resin and placed in a 60°C oven for 48 hours to cure. Thin sections were then cut using a Reichert – Jung Ultracut E Ultramicrotome with a diamond knife (approximately 100nm thick). The spinal cord sections were cut 2 mm away from each side of the visible lesion site. They were then placed on 300 mesh copper grids which were then stained as follows:

2% Aquous Uranyl Acetate – 10 minutes, 2 x 5 minutes distilled water rinse

Lead Citrate – 4 minutes, Quick rinse with distilled water, Air Dry

The samples were then viewed using a JEOL JEM 1230 Transmission Electron Microscope at 80 kV. Images were captured using a Hamamatsu ORCA-HR digital camera.

3.2.3 TEM Mitochondria Analysis

Two coronal sections were cut for each mouse SC on either side of the visible lesion site and placed onto a viewing grid. For each mouse 400 mitochondria were counted and classified as either healthy or damaged (200 mitochondria per grid). To ensure a representative sample of mitochondria were being counted and minimize regional bias, each section was divided into four

quadrants and at least 50 mitochondria were counted in each. This ensured that mitochondria were being counted from all regions of the section. Mitochondria were only counted in myelinated axons which are easily identifiable in electron micrographs due to the dark concentric rings of the myelin sheath surrounding them. Mitochondria visible outside of the myelinated rings were not considered as it would be very difficult to determine if they were within a neuron or supporting cell (glia). Each image was counted in its entirety to avoid sampling bias and therefore some quadrants had more than 50 total mitochondria counted. A total of 155 electron micrographs for control specimens and 142 electron micrographs for Ru265 treated samples were counted (total of 4 animals per group). Data from the mitochondrial counting experiments were analyzed by unpaired t-tests. Due to the subjective nature of classifying mitochondria as healthy or damaged, the analysis was performed by a second individual that had no prior knowledge of the study objectives and image file names were removed. The secondary individual's healthy and damaged mitochondrial data did not pass the D'Agostino & Pearson normality test and was therefore analysed using the Mann-Whitney U test. For all analyses the alpha value was set to 0.05. GraphPad Prism (version 9.0) was used to perform all statistical analyses.

3.2.4 Fluoro-Jade C and Immunohistochemistry Sample Preparation & Processing

Four control mice and eight treatment mice (Thy1-YFP B6.Tg.Cg. 16Jrs/J of C57BL/6J background) were used to evaluate neuronal survival. This strain expresses YFP at high levels in motor and sensory neurons allowing for visualization of labelled axons. YFP emits light at a similar wavelength to FJC, at ~520nm. However, when auto-contrast was removed there was no visible YFP present in all samples. All mice received a moderate tSCI and were given either PBS

or Ru265 epidurally (0.025 mg/kg). Mice were euthanized as previously described and the spinal cord of each mouse was isolated by laminectomy and placed into 4% PFA in PBS overnight followed by 15% and then 30% sucrose for at least 24 hours (until sunk). The tissue was cut (Figure 13) immediately on either side of the visible hematoma/lesion site and embedded in OCT compound (Fisher #4585, VWR # 95057-838) (Figure 13). 25 µM coronal sections were then cut using a cryostat (LEICA CM1950) set to -25°C and placed onto gelatin-coated slides.

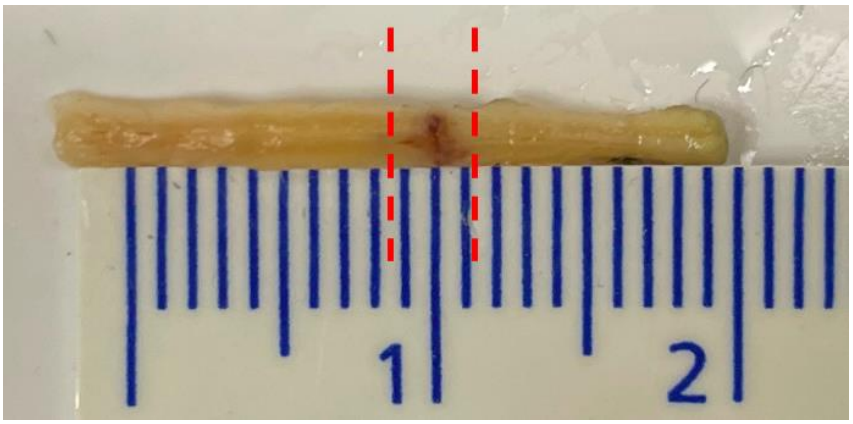

Figure 13: An injured spinal cord 4 hours post-impact isolated by serial laminectomy. The hematoma indicates the primary injury with its boundaries being indicated by the dotted red lines. To avoid cutting within the primary injury sectioning began immediately outside the dotted lines.

3.2.5 Fluoro-Jade C & Hoechst Labelling

Sections on slides with SC sections were dried at 55°C for 1 hour to ensure good adhesion and drying. A basic alcohol solution (50 mL) was placed into a Coplin jar and sections were incubated for 5 minutes, then transferred to a Coplin jar containing 70% ethanol for 2 minutes and rinsed. A solution of 0.06% potassium permanganate solution (Sigma Aldrich, #223468) was prepared to minimize fluorescent background signals, and slides were immersed for 10 minutes. To stop staining the sections were then rinsed for 2 minutes in distilled water. A

0.01% working solution of Fluoro-Jade C (Histo-Chem Inc., USA) was prepared and 1 mL of 0.01% Hoechst (Invitrogen, H21492) a nucleic acid stain, was added to the Coplin jar. Sections were incubated in this solution for 15 minutes. Following staining, the sections were rinsed in distilled water for 3 minutes and dried using a slide warmer at 50-60°C for 10 minutes in the dark. They were cleared by immersing in xylenes for 2 minutes and cover slipped with DPX (Sigma-Aldrich, #06522).

3.2.6 Double Labelling with FJC & NeuN Immunolabelling

For antigen retrieval, sections on slides were brought to a boil in 10 mM sodium citrate buffer (pH 6.0), then maintained at a sub-boiling temperature for 10 mins and subsequently cooled for 30 mins on the benchtop. Spinal cord sections were incubated in blocking buffer (1X PBS/5% normal goat serum/0.3% TritonX-100) for 1 hour. While blocking, the primary antibody, Rb mAB to NeuN (Abcam, ab177487) was prepared by diluting with antibody dilution buffer (1X PBS/1% BSA/0.3% TritonTMX-100, pH 7.2) at a 1:500 ratio. The blocking solution was aspirated using a pipette and the primary antibody solution was applied and incubated at 4°C overnight. The sections were then thrice rinsed in PBS for 5 mins and incubated in fluorochrome-conjugated secondary antibody (excitation: 590 nm, emission: 617 nm), Goat pAB to Rb (Alexa Fluor 594-conjugated, ab207279) and diluted in antibody dilution buffer (1X PBS/1% BSA/0.3% TritonX-100, pH 7.2) for 2 hours at room temperature in the dark. After rinsing with PBS, and incubating in 0.06% potassium permanganate for 10 minutes, the sections were again rinsed in PBS and placed into 0.01% FJC working solution for 15 minutes. After being dried on a slide warmer for 30 minutes, the sections were coverslipped using DPX.

3.2.7 FJC Imaging and Analysis

All fluorescence images were captured using a Zeiss Axio Imager Z2 with a monochrome camera. For counting purposes, all images were taken at 20X objective within the same region of the SC as shown in Figure 14. To consistently find the counting region the central canal was located, and the stage was automatically moved 3 high power fields to the left and one high power field dorsally. This region comprises lamina V which relays sensory, including nociceptive information. A total of 27 sections were counted in the control group and 44 were counted in the treatment group. FJC positive cells were counted using the Cell Counter plugin on Image J 2.3 (Kurt de Vos, University of Sheffield, Academic Neurology). This plugin tracks the cells as they are counted by placing a marker on them and gives a read-out of the total number of cells counted. The FJC control data was not normally distributed following the D'Agostino & Pearson normality test and therefore this data was analyzed using the non-parametric Mann-Whitney U test.

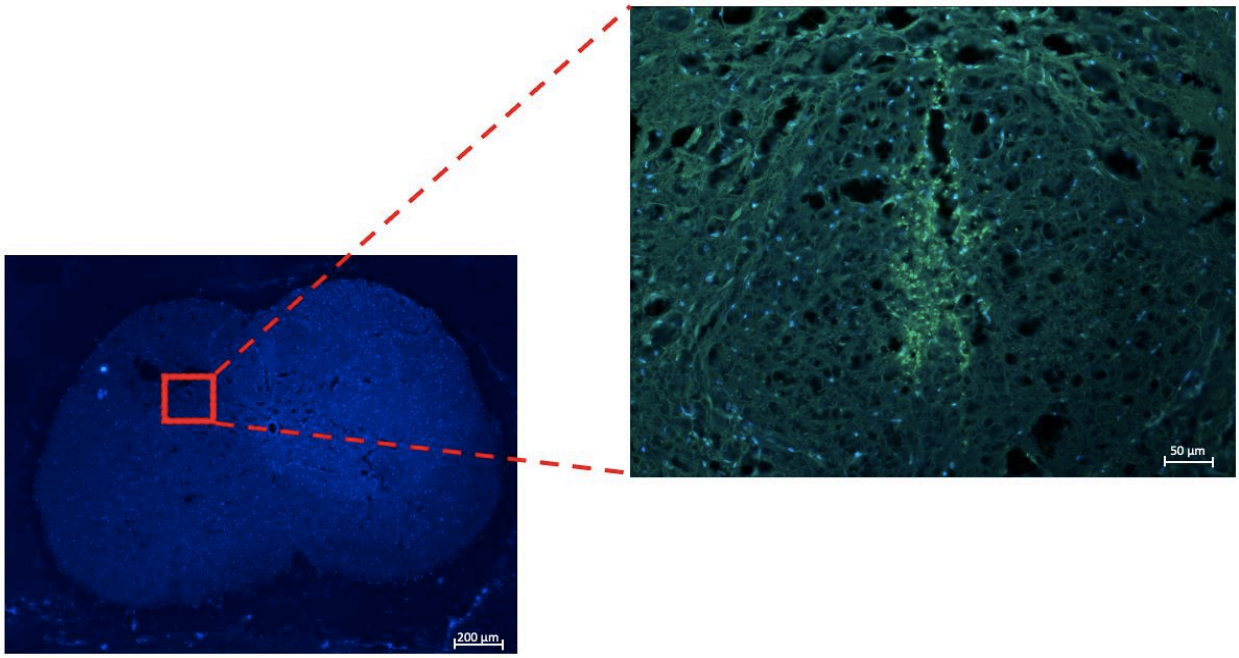

Figure 14: A spinal cord section (left) imaged using low power objective indicating the region of interest for counting FJC + Cells. The panel on the right is the selected region shown using a 20X objective with FJC + cells (green) clustered centrally in this area.

3.3 Results

3.3.1 Evaluation of Impact Parameters

Animals were observed to have similar results in regards to their response to SC impact. Upon delivery of the impact animals had immediate spastic contraction of the lower extremities confirming the injury was delivered. The two primary impact parameters indicative of injury severity: force and displacement, were plotted and found to be clustered in both control and Ru265 treated animals (Appendix: Figure 23). Additionally, both force and displacement values in control and Ru265 treated animals were found to be not statistically different from one another (force: $t(18)=1.265$, $p=0.2218$, displacement: $t(18)=0.2369$ $p=0.8154$) (Appendix: Figures 24 and 25). This suggests that the injuries delivered between control and Ru265 treated animals were comparable. Furthermore, histological evaluation of control and Ru265 treated sections revealed similar cytoarchitecture disruption at the level of the lesion (Appendix: Figure 26).

3.3.2 Evaluation of Mitochondrial Structural Integrity following tSCI

While imaging, an arbitrary scale of mitochondrial integrity was established in order to facilitate classification of healthy or damaged mitochondria. Using the scale, it was established that healthy mitochondria appear electron dense, with compact cristae and intact membranes (Jia et al., 2016). As the mitochondria become increasingly damaged, they appear more electron transparent, the cristae become diffuse and disorganized, and their membranes may be ruptured (Jia et al., 2016; Giacci et al., 2018) (Figure 15). It should be noted that assessment of mitochondrial viability was an all-or-none phenomena. Once mitochondria display early (visible) damage they are not able to recover and will gradually progress to death (Tang et al., 2021).

Therefore, when counting mitochondria they were classified as either healthy or damaged (included early damage and anything past this on the scale).

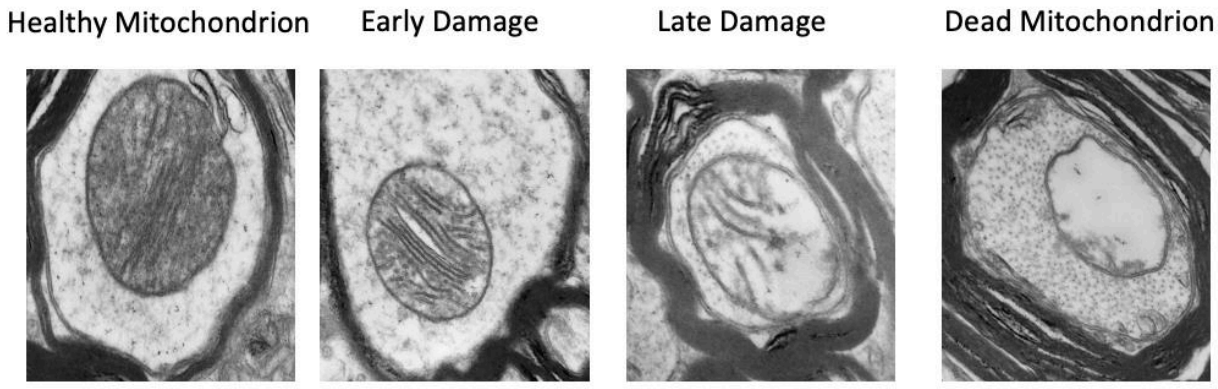

Figure 15: Scale of mitochondrial degradation observed using transmission electron microscopy following tSCI.

Control specimens were observed to have an increase in damaged mitochondria compared to those treated with Ru265. Mitochondria in control sections appeared much more electron transparent and had very sparse and diffuse cristae compared to treated samples. Treated samples had a notable increase in electron dense mitochondria with compact cristae indicating maintained structural integrity. Using the previously described scale of mitochondrial degeneration, the red arrowheads in the control panel would be classified as dead, the yellow arrowhead mitochondria exhibits early damage, and the one indicated by the green arrow would be considered healthy (Figure 15).

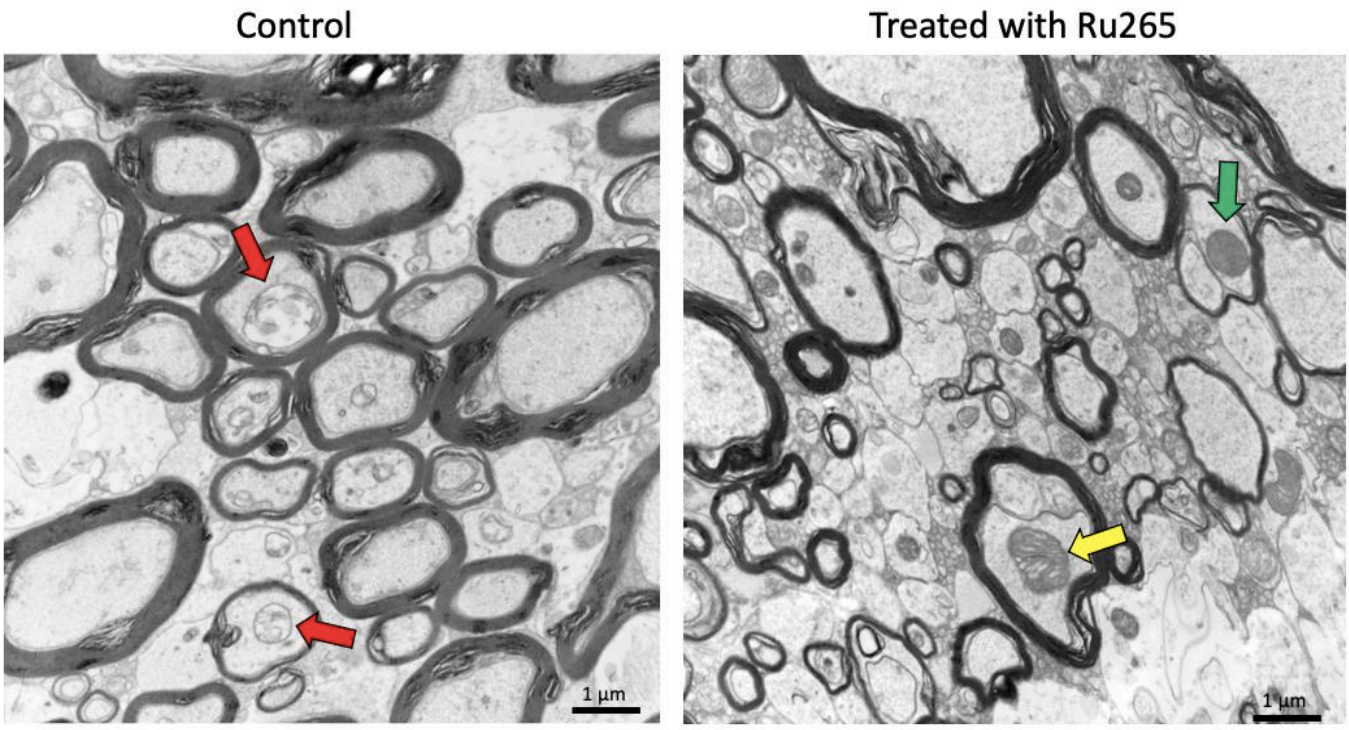

Figure 16: Electron micrographs of control and Ru265 treated SC sections 4h following tSCI. Mitochondria in the control section appear electron transparent with diffuse cristae (indicated by red arrowheads). Mitochondria in treated samples are more electron dense with compact cristae (yellow arrowhead indicates early damage, green indicates healthy mitochondria).

Normality was assessed prior to performing t-tests using the Shapiro-Wilk normality test. Both sets of mitochondria data (damaged and healthy) passed the normality tests, having p-values that were not significant (healthy: control ($p=0.9985$), treatment ($p=0.1399$), damaged: control ($p=0.7606$), treatment ($p=0.3445$). The number of mitochondria that classified as healthy was found to be significantly higher in mice treated with Ru265 compared to control specimens ($p<0.0001$) (Figure 17). Results are expressed as mean ± standard error of the means (SEM). The mean number of healthy mitochondria (counted in fields of equal size) in specimens treated with Ru265 was 274.5 ± 14 whereas in control mice it was 120 ± 6. These findings suggest the mitochondria have better structural integrity with Ru265 treatment.

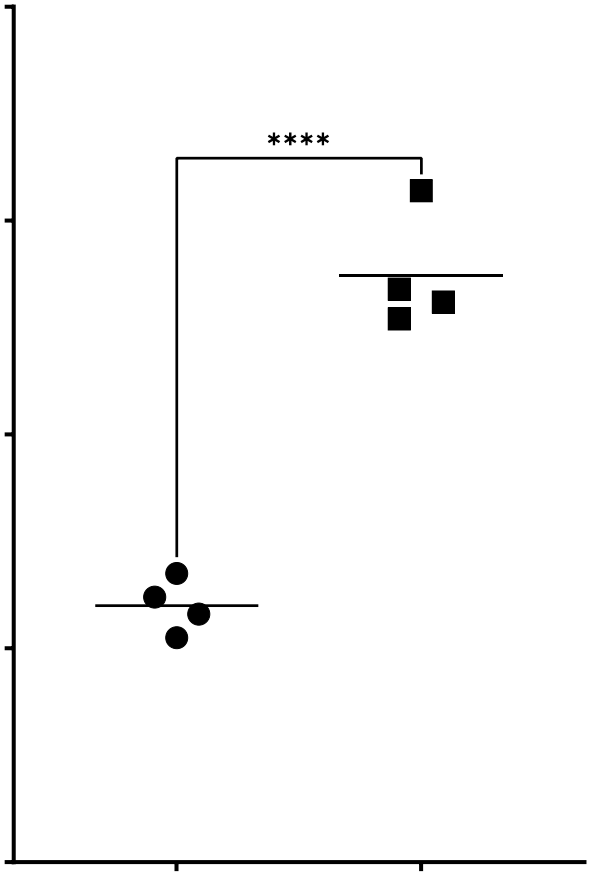

Figure 17: Number of healthy mitochondria in control vs treatment samples 4h following tSCI. $t(6)=10.38$, $p<0.0001$. Horizontal lines represent the mean.

The number of damaged mitochondria was found to be significantly higher in control mice compared to mice treated with Ru265 ($p<0.0001$) (Figure 18). The mean number of damaged mitochondria counted in control specimens was 326.3 ± 6 and in treated samples it was 167 ± 6. This supports the previous finding about healthy mitochondria and provides further evidence that Ru265 is mitoprotective following tSCI.

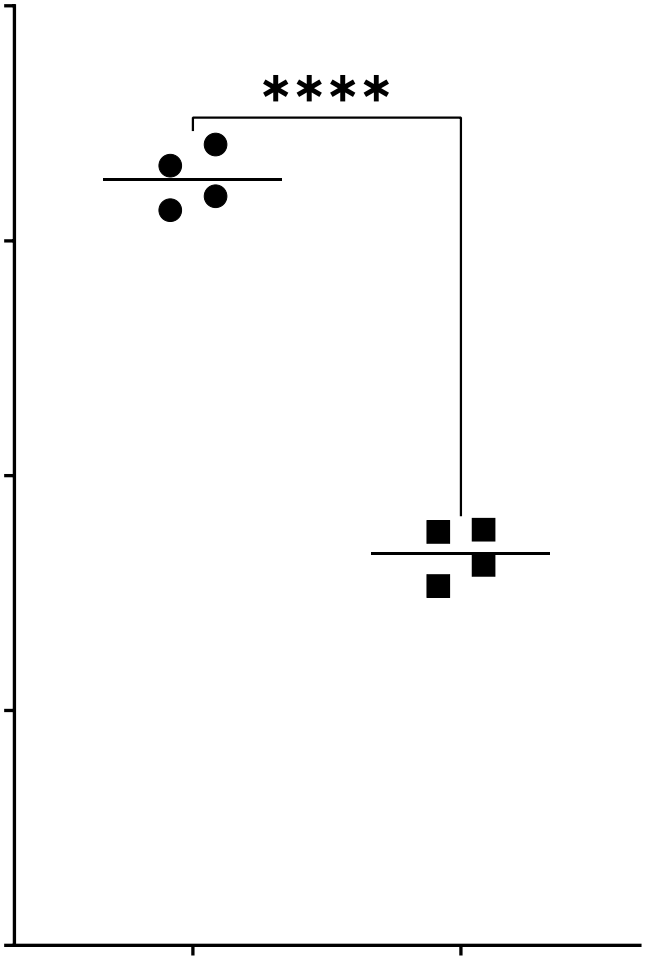

Figure 18: Number of damaged mitochondria in control vs treatment samples 4h following tSCI. $t(6)=18.95$, $p<0.0001$. Horizontal lines represent the mean.

A volunteer with no prior knowledge of the study and blinded to experimental conditions also evaluated mitochondrial integrity using the same electron micrographs and classified them as either healthy or damaged. The results were consistent with what was previously reported with marginal differences. Normality was assessed prior to performing t-tests using the Shapiro-Wilk normality test. Both sets of mitochondria data (damaged and healthy) passed the normality tests, having p-values that were not significant (healthy: control ($p=0.4492$), treatment ($p=0.0787$), damaged: control ($p=0.7168$), treatment ($p=0.7178$). Therefore, data was analyzed with an unpaired t-test. Similar to the data analyzed prior, Ru265 treated specimens had significantly more numerous healthy mitochondria ($p<0.0001$) and significantly fewer damaged mitochondria ($p<0.0001$) (Figure 19).

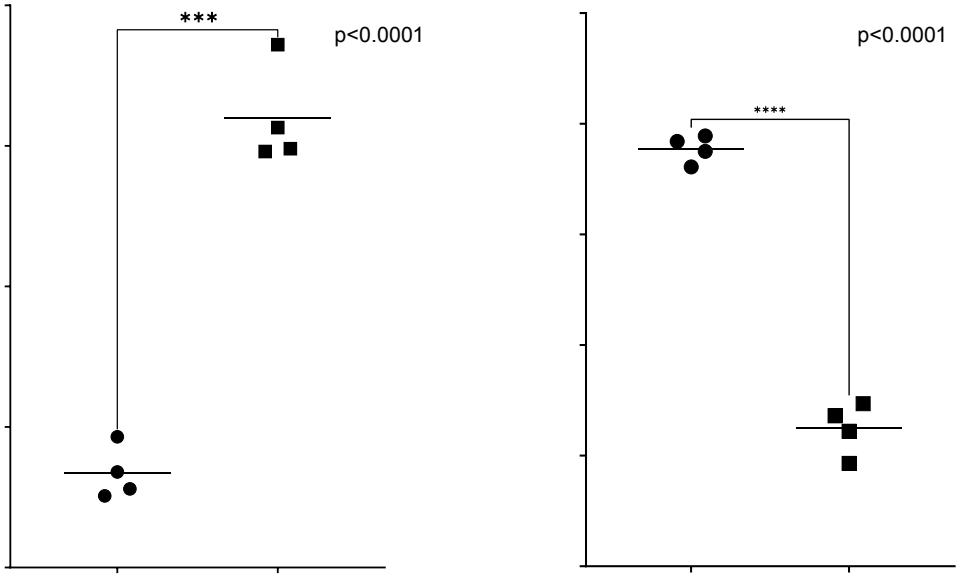

***Figure 19**:* Number of healthy and damaged mitochondria in control vs treatment samples. This data was generated by another unbiased individual to account for the subjective nature of the healthy vs damaged classification process. Horizontal lines represent the mean. Left: $t(5)=12.55$, $p<0.0001$. Right: $t(5)=19.15$, $p<0.0001$.

3.3.3 NeuN Immunolabelling

Prior to evaluating neuronal damage using FJC, its specificity as a neuronal marker in the SC was first confirmed by triple labelling with FJC, Hoechst and NeuN. Panels A-D in Figure 20 demonstrate that in regions of the section where FJC is not present (indicating lack of degenerating neurons) (panel D), Hoechst and NeuN label healthy cells. Whereas, in another region (panel H) a neuronal cell body and a portion of its dendrites are labelled with FJC. Supporting that FJC is specific to labelling neurons both NeuN (panel F) and Hoechst (panel G) both exhibit strong labelling to the neuron. These findings confirm that FJC is specific to labelling neurons in the SC.

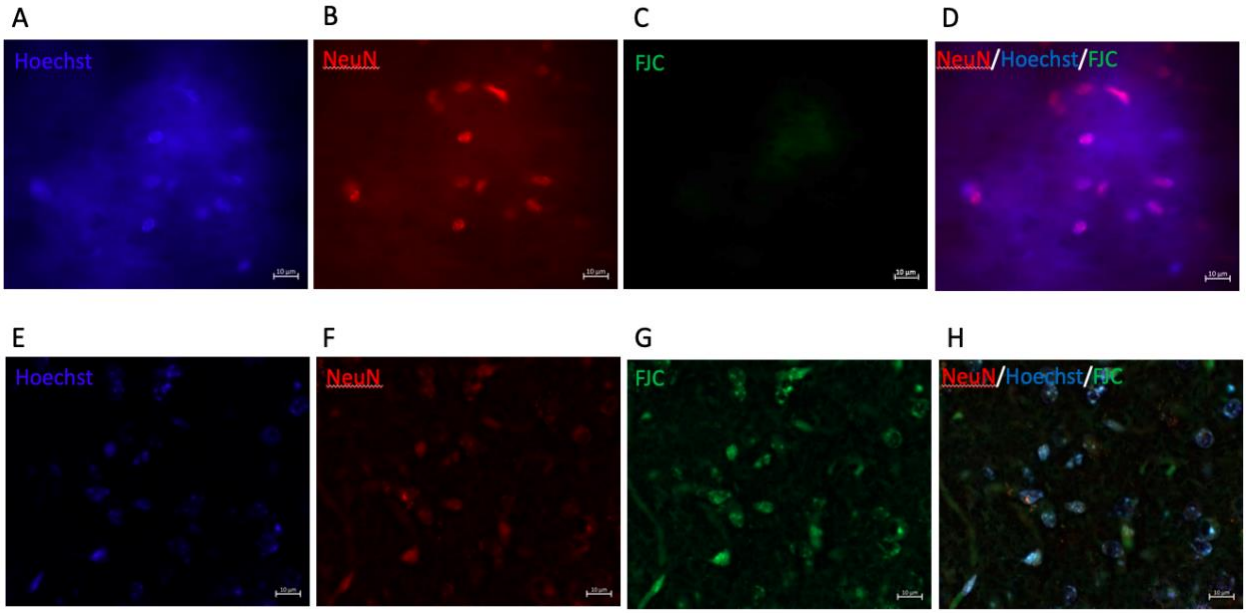

Figure 20: Fluorescence microscopy showing colocalization of FJC, Hoechst, and NeuN. Panels A-D show a region with NeuN and Hoechst labelleling neuronal cell bodies, but no FJC labelling is present. Panels E-H show a degenerating neuron labelled with NeuN, Hoechst, and FJC. These images demonstrate the specificity of FJC as a label for neuronal degeneration. All images were taken under 100X oil immersion objective, scale bar=10 µm.

3.3.4 Evaluation of Neurodegeneration with Fluoro-Jade C Labelling

Qualitative illustrations of the FJC labelling results are shown in Figure 21. The left panel corresponds to a control mouse and the right panel a mouse treated with Ru265. The control section has noticeably more FJC + neurons (179) compared to the Ru265 treated section (108), suggesting less neuronal degeneration in the treated animal. These images are representative of the trends observed and were selected for this reason.

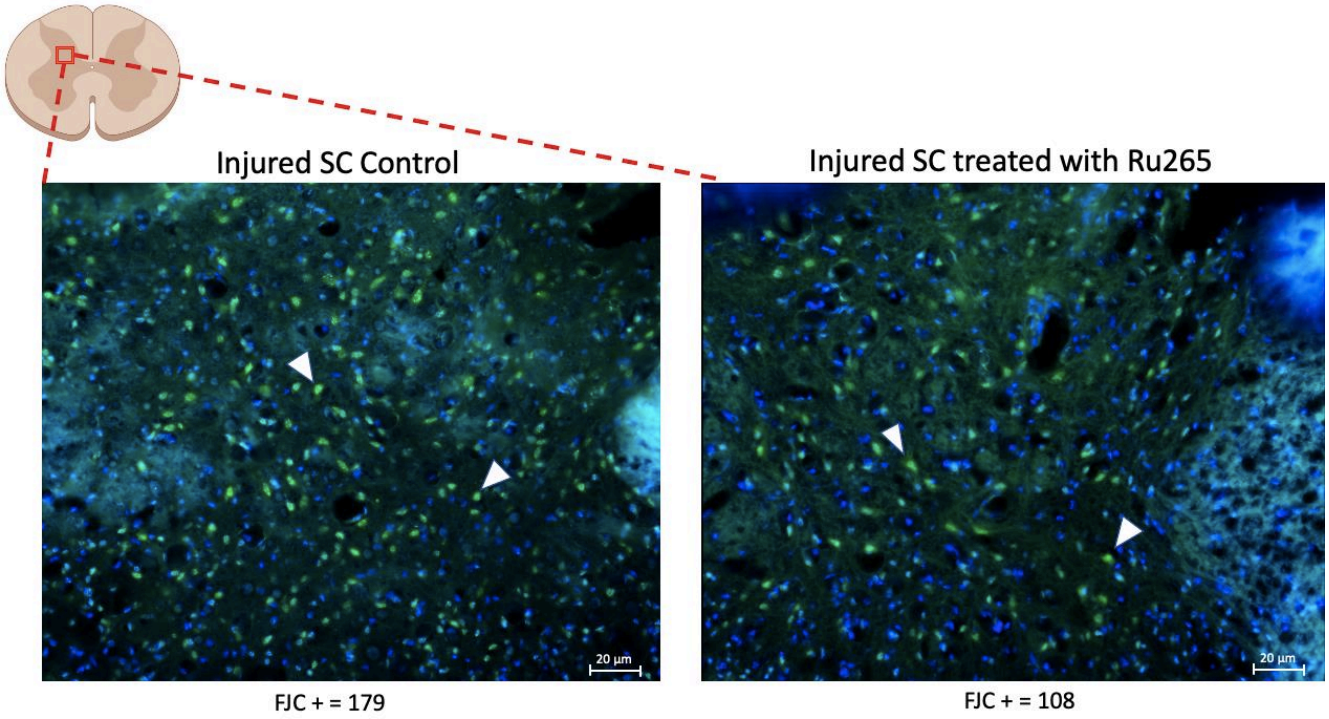

Figure 21: Fluorescence images of a control (left) and Ru265 treated (right) SC section (40X magnification). Arrows indicate FJC+ cells.

The FJC control data was found to be normally distributed following the Shapiro-Wilk normality test and therefore this data was analyzed using an unpaired t-test (control: (p=0.0725), treatment: (p=0.8624). Analysis of counted FJC sections revealed that mice treated with Ru265 had significantly fewer positively labelled FJC cells when compared to control mice (t(9)=3.373,

p=0.0079). This indicates that with treatment of Ru265 there is less neuronal degeneration following SCI compared to untreated mice. The mean number of FJC + neurons (± SEM) in control mice (in 20X field) was 547 ± 35 neurons whereas in mice treated with Ru265 it was 365 ± 41 neurons (Figure 22).

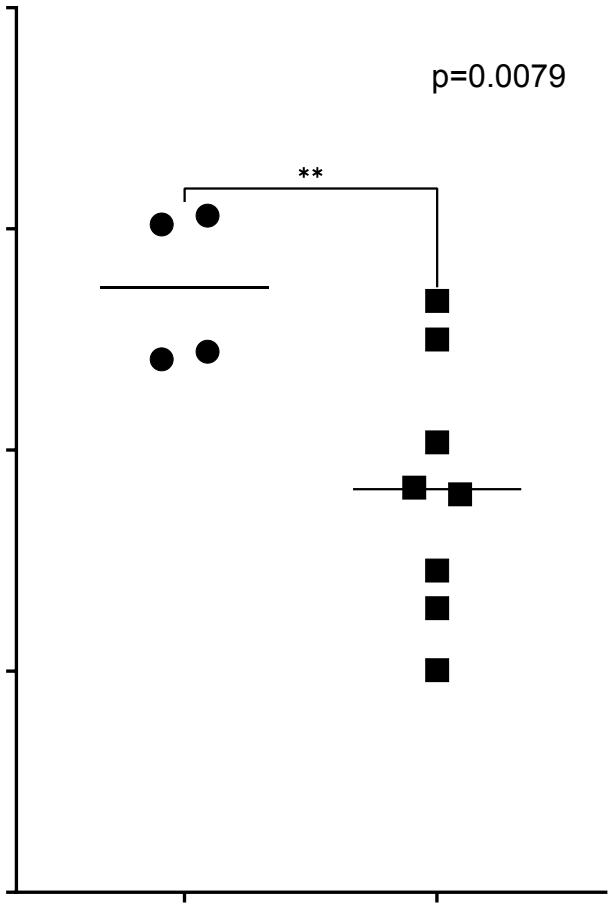

***Figure 22**:* Degenerating neurons in treatment vs control samples 72h following tSCI. Horizontal lines represent the mean. (t(40)=3.609, p=0.0008, two-tailed).

3.4 Discussion

In this chapter, the potential mitoprotective and neuroprotective effects of Ru265 were investigated. Ru265 elicits its effects by inhibiting the MCU on the IMM, and therefore mitochondria were examined in control and treatment specimens to determine if the drug was indeed preserving mitochondrial structural integrity following traumatic injury, as predicted. By counting the number of both healthy and damaged mitochondria in control and Ru265 treated SC sections, it was found that there are significantly more mitochondria classified as healthy in Ru265 treated sections. Supportively, Ru265 treated sections had significantly less mitochondria that were classified as damaged. These findings suggest that Ru265 treatment provides mitoprotection following tSCI. Mitochondria-target therapies have been widely researched in previous studies, with a new emphasis on targeting biogenesis, which is the synthesis of new mitochondria to replace those being damaged by SCI (Simmons et al., 2022). Other heavily researched mitochondrial therapies for SCI include mPTP inhibitors, antioxidants, and alternative energy sources ('biofuels' help to replace energy sources that are depleted following SCI) (Scholpa and Schnellmann, 2017). A significant drawback to these therapies is that they are not consistently effective as standalone treatments of SCI (Scholpa and Schnellmann, 2017). As SCI is a complex condition comprised of several pathways, even in just the mitochondrial context, targeting just one pathway is likely not enough to mitigate all the simultaneous injury cascades. Researchers are now pushing for multiple mitochondrial-targeted therapies that could be used together to provide a more effective treatment (Scholpa and Schnellmann, 2017). In future studies, MCU inhibitors such as Ru265 should be used in conjugation with other mitochondrial therapies to maximize the benefits of this approach.

After establishing that Ru265 has mitoprotective effects following SCI, neuronal survival was evaluated with fluorescence microscopy. FJC labelling demonstrated significantly fewer degenerating neurons in SC sections treated with Ru265 compared to controls. This suggests that Ru265 provides neuroprotection following tSCI.

Together, these observations support the potential of Ru265 as a neuroprotectant mediated through mitochondrial preservation. Although there may be pharmacodynamic effects not yet elucidated, the current results are consistent with previous work indicating that the mechanism of action is through inhibition of the MCU, thereby reducing the deleterious effects of massive Ca^{2+} influx into mitochondria. Overall, these findings suggest that MCU inhibitors are a promising avenue of mito- and neuro-protection following tSCI that should be further investigated in future studies aimed at the discovery of more clinically tolerable compounds, which mitigate the pro-convulsant effects of Ru265 whilst amplifying the therapeutic effects.

4.0 GENERAL DISCUSSION

4.1 Local delivery of Ru265 by Epidural Application

Due to the observed seizure-like behaviors following IP injection of Ru265, epidural application of the drug was evaluated as a localized method of drug delivery (and concomitantly, a reduced total dose) in an attempt to mitigate these effects. Achieving effective tissue concentrations and minimizing drug spillover to healthy/uninjured tissue were also major considerations. Based on a previous study, for the drug to be effective concentrations between 0.026 and 0.315 μM are required. Even the lowest concentration observed within the SC at 4h post-impact was above this range (0.54 μM) (Novorolsky et al., 2020). Due to the small sample sizes used in this study, performing statistical analyses was not appropriate due to lack of power. However, the primary intention using this method of drug delivery showing that Ru265 is able to penetrate into the injured SC at effective concentrations was answered positively. There was notably more Ru265 found in the spinal parenchyma following epidural application (~11X increase) compared to when the drug was administered via IP injection. The 4 and 8-hour time points had notably less Ru265 circulating systemically with epidural delivery, however; at 24 hours the values for both drug delivery methods had just marginal differences in the blood, likely due to Ru265 being excreted renally. Concentrations found in the forebrain were very similar at all time points with both methods of drug delivery, likely due to a combination of Ru265 entering the circulation through broken blood vessels and via the CSF in the sub-arachnoid space.

This experiment suggested that epidural delivery of Ru265 allows for a higher concentration of the drug to penetrate the injured spinal cord parenchyma with a lower systemic

concentration, where it can elicit undesirable side effects. Localized methods of drug delivery are critical because they provide high and sustained local concentrations of drugs without the large systemic concentrations, therefore minimizing systemic toxicity (Wen et al., 2015). Epidural delivery was chosen as the method of drug delivery over other commonly used local drug delivery methods such as intrathecal (injection into the subarachnoid space) or intraparenchymal injection to the SC due to safety considerations. Intrathecal injections have not yet been optimized in mice as they have with rats and often lead to injury, paralysis, or mortality (Oladosu et al., 2016). This is likely due to the fact that there are notably fewer studies using intrathecal injection in mice due to their smaller gross anatomy making the intrathecal injection increasingly complex with a higher risk of error (Kim et al., 2020). Intraparenchymal injection directly disturbs SC tissue and causes cell death by shearing stress in the region of entry (Ahuja et al., 2020). For these reasons, epidural delivery was considered the least invasive and also least potentially harmful method of Ru265 delivery. Future experiments should increase the sample sizes and perform statistical analyses to validate the results found in this study.

A limitation of this study is that the suspension/slurry of Ru265 placed onto the dura matter had low viscosity. This allowed some drug to flow from the impact site, in some instances due to the nature of the anatomy in this region, potentially hindering the efficacy of the drug delivery. The high degree of curvature in the spine at the T10 vertebral level may have also contributed to variances due to the drug being applied onto an uneven sloping surface (Harrison et al., 2013). Some of the drug could also be flowing out of the impact region due to bleeding, or getting trapped due to clotting, the amount of which varied between mice depending on the surgery. Effectively, due to these reasons we could not ensure that the entire mass of the drug stayed in place following application. This leaves a need for consideration of better drug

formulations. Future studies using epidural delivery of drugs should consider mixing the drug of interest with a higher viscosity liquid such as a biocompatible oil or paste. Such optimization could likely also enable achieving an even lower total dose than the current 1mg/kg which is already just 33% of the previously published values. Recent studies have also suggested that hydrogel-based drug delivery systems are an excellent model for localized drug delivery (Pakulska et al., 2012; Baumann et al., 2017; Shultz and Zhong, 2021). Hydrogels are cross-linked polymers consisting of hydrophilic or amphiphilic material that can be optimized to deliver therapeutics based on the application it will be used for (Parhi, 2017).

A hydrogel could be particularly effective in a SCI model applied epidurally because previous studies have shown that they also provide the added benefits of structural support and guidance for regeneration (Shultz and Zhong, 2021). When applied epidurally following a laminectomy the hydrogel would sit directly above the injured tissue where regeneration and support is most needed. These hydrogels can be modified by altering pore-size to allow for a more sustained drug release that will allow the drug to remain in effect for longer periods of time (Li and Mooney, 2016). A previous study injected a drug-infused hydrogel directly onto a hemi-sected SC in a combined epidural and intra-parenchymal delivery method and they observed increased neuroprotection and locomotor recovery following injury (Liu et al., 2016). Hydrogels are a promising method of localized drug delivery following tSCI and applied epidurally to delivery Ru265 could maximize the benefits of this drug. Future studies should confirm the validity of epidural delivery as a method of local drug delivery to the SC with improved drug formulations and an increased number of animals to confirm the promising data shown in this experiment.

4.2 Mitoprotective and Neuroprotective effects of Ru265

The establishment of the drug delivery model was followed by an investigation of Ru265's potential mitoprotective effects. Using TEM, mitochondria in control and Ru265 treated samples were classified as healthy or damaged. With all mitochondria counted it was determined that there were significantly more numerous healthy mitochondria and significantly fewer damaged mitochondria in Ru265 treated samples. This suggests that Ru265 improves mitochondrial integrity following SCI by blocking the MCU and inhibiting calcium overload triggered by excitotoxicity. When mitochondria are damaged, they become extremely reactive, damaging themselves, surrounding mitochondria and the cell as a whole (Goodman, 2021). Essentially, mitochondria act as a 'death switch' by sensing any pathological stressors in the cell and initiating apoptosis when homeostasis cannot be maintained (Duchen, 2000). Apart from not activating the 'death switch', maintaining mitochondrial integrity and function is equally if not more important to sustain ATP supply to fuel neuronal function and repair. Therefore, it is critical to investigate potential therapeutics that can help maintain the physiological homeostasis of these cells following SCI, such as Ru265 or similar MCU inhibitors. Considering Ru265 levels remained high up to 24 hours following injury, later timepoints should be considered to see if there are beneficial effects apart from the 4-hour timepoint that was tested.

A limitation of this study to consider is that only female mice were used for all experimental procedures. Female mice were chosen due to the lowered risk of complications during recovery following tSCI. Due to impaired input from the autonomic nervous system following injury, bladder function is disrupted, and mice need to be manually expressed up to a week following injury (Wada et al., 2017). In male mice this is much more difficult and can often lead to fatal complications such as bladder rupture and urethral blockage (Lilley et al.,

2020). Due to these animal welfare considerations female mice were chosen to be used for all procedures. However, it should be noted that in humans males are more likely to suffer from SCIs compared to females (~80% of cases are in males) and therefore male mice would have been more representative of the affected population (Raguindin et al., 2021). Additionally, some studies suggest that female sex hormones (particularly estrogens) have been shown to exert some neuroprotective effects in the brain (Brann et al., 2007). This likely would have minimal effects on our results but is important to disclose, nonetheless. Future studies should consider comparing the effectiveness of Ru265 in both male and female mice following tSCI.

As a proof of principle experiment, the mitoprotective effects of MCU inhibition could be further verified by performing similar experiments on a new line of transgenic mice that have a tamoxifen-induced MCU knockout in Thy-1 expressing neurons (Nichols et al., 2018). This model was used in a previous study that gave the MCU knockout mice a hypoxic/ischemic (HI) brain injury (Nichols et al., 2018). Their results showed that HI-induced sensorimotor deficits, neuronal death, and mitochondrial damage were decreased in the knockout mice compared to controls (Nichols et al., 2018). Confirming the mitoprotective and neuroprotective effects of MCU inhibition using such a model would provide further evidence that MCU inhibitors have the potential to be highly efficacious neuroprotectants for treatment of tSCI, and further support the mechanism of action of Ru265 tSCI.

With promising mitoprotection observed with Ru265 treatment, its effects on neuronal survival were evaluated next. Using FJC as a label for neuronal degeneration, the number of labelled cells were compared between Ru265 treated and control specimens. It was demonstrated that Ru265 treated samples had significantly fewer labelled neurons indicating that treatment with Ru265 reduces neuronal degeneration following tSCI. These data suggest that Ru265 is a

promising neuroprotectant which should be further studied. However, due to the observed seizure behaviors following administration, it is unlikely that this compound will be translated clinically without drastic improvements in localizing the drug to the spinal cord lesion site to keep it out of the circulation. Another emerging field that could mitigate these effects by improving local delivery would be to use nanoparticle encapsulation. In this process the drug is encapsulated in a cavity surrounded by a polymer membrane that can be modified to deliver drugs to suit their intended purpose (can improve solubility and be modified for sustained drug release) (Singh and Lillard, 2009). Nonetheless, the findings in this study support that MCU inhibitors should be further investigated as neuroprotectants following tSCI. To our knowledge, this study is the first to evaluate the neuroprotective properties of an MCU inhibitor following tSCI. This indicates that there is a vast potential for further research to take place into these compounds and also synthesize similar compounds with better safety profile and tolerance.

Future studies should evaluate if the observed mitoprotective and neuroprotective effects of Ru265 translate into improvements in other SCI modalities such as improvements in chronic pain following injury, autonomic function (respiratory, cardiovascular, bowel and urinary complications, etc.), and motor evaluation. Behavioural analyses such as the Basso-Beattie-Bresnahan (BBB) and the Basso Mouse Scale (BMS) could be used for motor evaluation. These scales use several gait parameters (joint movement, trunk stability, coordination, etc.) to produce an overall score indicative of motor ability (Basso et al., 2006). The drawback with these scales is their subjective nature and therefore, computerized methods of gait analyses should also be considered. One of these methods includes angular kinematic analysis which uses high-speed cameras to capture coordinates of reflective markers attached to the animal's skin to track gait patterns (Battistuzzo et al., 2016). Footprint analysis is also highly established in the literature

and uses animals with inked paws walking across a piece of paper which can then be analyzed with computer software evaluating parameters such as limb rotation, stride length, base of support, etc. (Mendes et al., 2015). Improvements in motor scores would further establish the promise that MCU inhibitors have as neuroprotectants.

4.3 Conclusions

The results derived from the studies conducted for this thesis provide support that epidural delivery is an effective and feasible method of drug delivery to the injured SC. Administration of Ru265 epidurally led to a significant improvement in mitochondrial integrity at 4 hours following injury. Neuronal degeneration was found to be significantly reduced in Ru265 treated specimens compared to controls, likely as a result of increased mitochondrial survival. Future studies should continue investigating the promising therapeutic effects of MCU inhibitors following tSCI.

.

BIBLIOGRAPHY

Ahuja CS, Mothe A, Khazaei M, Badhiwala JH, Gilbert EA, van der Kooy D, Morshead CM, Tator C, Fehlings MG (2020) The leading edge: Emerging neuroprotective and neuroregenerative cell-based therapies for spinal cord injury. Stem Cells Transl Med 9:1509–1530.

Ahuja CS, Wilson JR, Nori S, Kotter MRN, Druschel C, Curt A, Fehlings MG (2017) Traumatic spinal cord injury. Nat Rev Dis Prim 3:17018.

Al Shoyaib A, Archie SR, Karamyan VT (2019) Intraperitoneal Route of Drug Administration: Should it Be Used in Experimental Animal Studies? Pharm Res 37:12.

Alizadeh A, Dyck SM, Karimi-Abdolrezaee S (2019) Traumatic Spinal Cord Injury: An Overview of Pathophysiology, Models and Acute Injury Mechanisms. Front Neurol 10:282.

Allen Ar (1911) Surgery Of Experimental Lesion Of Spinal Cord Equivalent To Crush Injury Of Fracture Dislocation Of Spinal Column: A Preliminary Report. J Am Med Assoc LVII:878–880.

Almad A, Sahinkaya FR, McTigue DM (2011) Oligodendrocyte fate after spinal cord injury. Neurotherapeutics 8:262–273.

Anjum A, Yazid MD, Fauzi Daud M, Idris J, Ng AMH, Selvi Naicker A, Ismail OHR, Athi Kumar RK, Lokanathan Y (2020) Spinal Cord Injury: Pathophysiology, Multimolecular Interactions, and Underlying Recovery Mechanisms. Int J Mol Sci 21:7533.

Bao Q, Shi Y (2007) Apoptosome: a platform for the activation of initiator caspases. Cell Death Differ 14:56–65.

Basso DM, Fisher L, Anderson A, Jakeman L, Mctigue D, Popovich P (2006) Basso, DM, Fisher, LC, Anderson, AJ, Jakeman, LB, McTigue, DM and Popovich, PG. Basso Mouse Scale for locomotion detects differences in recovery after spinal cord injury in five common mouse strains. J Neurotrauma 23: 635-659. J Neurotrauma 23:635–659.

Battistuzzo CR, Rank MM, Flynn JR, Morgan DL, Callister R, Callister RJ, Galea MP (2016) Gait recovery following spinal cord injury in mice: Limited effect of treadmill training. J Spinal Cord Med 39:335–343.

Baumann MD, Stanwick JC, Donaghue IE, Shoichet MS (2017) 7.31 Biomaterials for Spinal Cord Repair. In (Ducheyne PBT-CBII, ed), pp 628–641. Oxford: Elsevier.

Belov Kirdajova D, Kriska J, Tureckova J, Anderova M (2020) Ischemia-Triggered Glutamate Excitotoxicity From the Perspective of Glial Cells. Front Cell Neurosci 14.

Brann DW, Dhandapani K, Wakade C, Mahesh VB, Khan MM (2007) Neurotrophic and neuroprotective actions of estrogen: basic mechanisms and clinical implications. Steroids 72:381–405.

Bratton SB, Salvesen GS (2010) Regulation of the Apaf-1-caspase-9 apoptosome. J Cell Sci 123:3209–3214.

Broekemeier KM, Krebsbach RJ, Pfeiffer DR (1994) Inhibition of the mitochondrial Ca2+ uniporter by pure and impure ruthenium red. Mol Cell Biochem 139:33–40.

Buss A, Pech K, Merkler D, Kakulas BA, Martin D, Schoenen J, Noth J, Schwab ME, Brook GA (2005) Sequential loss of myelin proteins during Wallerian degeneration in the human spinal cord. Brain 128:356–364.

Carlson BM (2014) Chapter 11 - Nervous System. In (Carlson BMBT-HE and DB (Fifth E, ed), pp 216–253. Philadelphia: W.B. Saunders.

Chazotte B (2011) Labeling nuclear DNA with hoechst 33342. Cold Spring Harb Protoc 2011:pdb.prot5557.

Cheriyan T, Ryan DJ, Weinreb JH, Cheriyan J, Paul JC, Lafage V, Kirsch T, Errico TJ (2014) Spinal cord injury models: a review. Spinal Cord 52:588–595.

Cramer GD (2014) Chapter 2 - General Characteristics of the Spine. In (Cramer GD, Darby Spinal Cord, and Ans (Third Edition) SABT-CA of the S, eds), pp 15–64. Saint Louis: Mosby.

De Stefani D, Raffaello A, Teardo E, Szabò I, Rizzuto R (2011) A forty-kilodalton protein of the inner membrane is the mitochondrial calcium uniporter. Nature 476:336–340.

Demirel Y, Gerbaud V (2019) Chapter 11 - Thermodynamics and Biological Systems. In (Demirel Y, Gerbaud VBT-NT (Fourth E, eds), pp 489–571. Elsevier.

Dong X, Wang Y, Qin Z (2009) Molecular mechanisms of excitotoxicity and their relevance to pathogenesis of neurodegenerative diseases. Acta Pharmacol Sin 30:379–387.

Duchen MR (2000) Mitochondria and calcium: From cell signalling to cell death. J Physiol 529:57–68.

Elmore S (2007) Apoptosis: a review of programmed cell death. Toxicol Pathol 35:495–516.

Fan M, Zhang J, Tsai C-W, Orlando BJ, Rodriguez M, Xu Y, Liao M, Tsai M-F, Feng L (2020) Structure and mechanism of the mitochondrial Ca2+ uniporter holocomplex. Nature 582:129–133.

Featherstone DE (2010) Intercellular glutamate signaling in the nervous system and beyond. ACS Chem Neurosci 1:4–12.

Fehlings MG, Theodore N, Harrop J, Maurais G, Kuntz C, Shaffrey CI, Kwon BK, Chapman J, Yee A, Tighe A, McKerracher L (2011) A phase I/IIa clinical trial of a recombinant Rho protein antagonist in acute spinal cord injury. J Neurotrauma 28:787–796.

Fujitsuka N, Ito F (1983) Uptake of Ruthenium Red by the Sensory Nerve Terminal of the Frog Muscle Spindle. Okajimas Folia Anat Jpn 60:1–15.

Giacci MK, Bartlett CA, Huynh M, Kilburn MR, Dunlop SA, Fitzgerald M (2018) Three dimensional electron microscopy reveals changing axonal and myelin morphology along normal and partially injured optic nerves. Sci Rep 8:3979.

Goldshmit Y, Banyas E, Bens N, Yakovchuk A, Ruban A (2020) Blood glutamate scavengers and exercises as an effective neuroprotective treatment in mice with spinal cord injury. J Neurosurg Spine SPI 33:692–704.

Goodman SRBT-GMCB (Fourth E ed. (2021) Chapter 5 - Mitochondria and Diseases. In, pp 139–156. Academic Press.

Gourdin M (2013) Impact of Ischemia on Cellular Metabolism. In (Aronow PDE-WS, ed), pp Ch. 1. Rijeka: IntechOpen.

Gray MW (2013) Mitochondria. In (Maloy S, Hughes KBT-BE of G (Second E, eds), pp 430–432. San Diego: Academic Press.

Gupta P, Lakes A, Dziubla T (2016) Chapter One - A Free Radical Primer. In (Dziubla T, Butterfield DABT-OS and B, eds), pp 1–33. Academic Press.

Harrison M, O'Brien A, Adams L, Cowin G, Ruitenberg MJ, Sengul G, Watson C (2013) Vertebral landmarks for the identification of spinal cord segments in the mouse. Neuroimage 68:22–29.

Hilton BJ, Moulson AJ, Tetzlaff W (2017) Neuroprotection and secondary damage following spinal cord injury: concepts and methods. Neurosci Lett 652:3–10.

Hyrc K, Handran SD, Rothman SM, Goldberg MP (1997) Ionized intracellular calcium concentration predicts excitotoxic neuronal death: observations with low-affinity fluorescent calcium indicators. J Neurosci 17:6669–6677.

Hyun-Eui K, Fenghe D, Min F, Xiaodong W (2005) Formation of apoptosome is initiated by cytochrome c-induced dATP hydrolysis and subsequent nucleotide exchange on Apaf-1. Proc Natl Acad Sci 102:17545–17550.

Ikenari T, Kurata H, Satoh T, Hata Y, Mori T (2020) Evaluation of Fluoro-Jade C Staining: Specificity and Application to Damaged Immature Neuronal Cells in the Normal and Injured Mouse Brain. Neuroscience 425:146–156.

Jhun BS, Mishra J, Monaco S, Fu D, Jiang W, Sheu S-S, O-Uchi J (2016) The mitochondrial Ca2+ uniporter: regulation by auxiliary subunits and signal transduction pathways. Am J Physiol Cell Physiol 311:C67–C80.

Jia Z-Q, Li G, Zhang Z-Y, Li H-T, Wang J-Q, Fan Z-K, Lv G (2016) Time representation of mitochondrial morphology and function after acute spinal cord injury. Neural Regen Res 11:137–143.

Jones B V (2017) Cord Cystic Cavities: Syringomyelia and Prominent Central Canal. Semin Ultrasound, CT MRI 38:98–104.

Ju G, Wang J, Wang Y, Zhao X (2014) Spinal cord contusion. Neural Regen Res 9:789–794.

Kalogeris T, Baines CP, Krenz M, Korthuis RJ (2016) Ischemia/Reperfusion. Compr Physiol 7:113–170.

Kamer KJ, Mootha VK (2015) The molecular era of the mitochondrial calcium uniporter. Nat Rev Mol Cell Biol 16:545–553.

Kausar S, Wang F, Cui H (2018) The Role of Mitochondria in Reactive Oxygen Species Generation and Its Implications for Neurodegenerative Diseases. Cells 7:274.

Kaya Y, Yildiz A (2019) Speedy/RINGO: a molecular savior in spinal cord injury-based neurodegeneration? Neuroimmunol Neuroinflammation 6:5.

Kayalioglu G (2009) Chapter 3 - The Vertebral Column and Spinal Meninges. In (Watson C, Paxinos G, Kayalioglu GBT-TSC, eds), pp 17–36. San Diego: Academic Press.

Kehrer JP (2000) The Haber–Weiss reaction and mechanisms of toxicity. Toxicology 149:43–50.

Kim H, Na DL, Lee NK, Kim AR, Lee S, Jang H (2020) Intrathecal Injection in A Rat Model: A Potential Route to Deliver Human Wharton's Jelly-Derived Mesenchymal Stem Cells into the Brain. Int J Mol Sci 21.

Kim KK, Adelstein RS, Kawamoto S (2009) Identification of Neuronal Nuclei (NeuN) as Fox-3, a New Member of the Fox-1 Gene Family of Splicing Factors * . J Biol Chem 284:31052–31061.

Kurutas EB (2016) The importance of antioxidants which play the role in cellular response against oxidative/nitrosative stress: current state. Nutr J 15:71.

Lau A, Tymianski M (2010) Glutamate receptors, neurotoxicity and neurodegeneration. Pflügers Arch - Eur J Physiol 460:525–542.

Lee JHT, Streijger F, Tigchelaar S, Maloon M, Liu J, Tetzlaff W, Kwon BK (2012) A contusive model of unilateral cervical spinal cord injury using the infinite horizon impactor. J Vis Exp:3313.

Lehrer S, Rheinstein PH (2019) Transspinal delivery of drugs by transdermal patch back-of-neck for Alzheimer's disease: a new route of administration. Discov Med 27:37–43.

Li J, Mooney DJ (2016) Designing hydrogels for controlled drug delivery. Nat Rev Mater 1.

Lilley E, Andrews MR, Bradbury EJ, Elliott H, Hawkins P, Ichiyama RM, Keeley J, Michael-Titus AT, Moon LDF, Pluchino S, Riddell J, Ryder K, Yip PK (2020) Refining rodent models of spinal cord injury. Exp Neurol 328:113273.

Little JP (2019) Chapter 22 - The spine: biomechanics and subject-specific finite element models. In (Scataglini S, Paul GBT-DHM and P, eds), pp 287–293. Academic Press.

Liu D, Jiang T, Cai W, Chen J, Zhang H, Hietala S, Santos HA, Yin G, Fan J (2016) An In Situ Gelling Drug Delivery System for Improved Recovery after Spinal Cord Injury. Adv Healthc Mater 5:1513–1521.

Liu D, Liu J, Wen J (1999) Elevation of hydrogen peroxide after spinal cord injury detected by using the Fenton reaction. Free Radic Biol Med 27:478–482.

Lu J, Ashwell KWS, Waite P (2000) Advances in Secondary Spinal Cord Injury: Role of Apoptosis. Spine (Phila Pa 1976) 25.

Lu P, Jones LL, Tuszynski MH (2007) Axon regeneration through scars and into sites of chronic spinal cord injury. Exp Neurol 203:8–21.

Mallilankaraman K, Doonan P, Cárdenas C, Chandramoorthy HC, Müller M, Miller R, Hoffman NE, Gandhirajan RK, Molgó J, Birnbaum MJ, Rothberg BS, Mak D-OD, Foskett JK, Madesh M (2012) MICU1 Is an Essential Gatekeeper for MCU-Mediated Mitochondrial Ca2+ Uptake that Regulates Cell Survival. Cell 151:630–644.

Mammucari C, Gherardi G, Rizzuto R (2017) Structure, Activity Regulation, and Role of the Mitochondrial Calcium Uniporter in Health and Disease. Front Oncol 7:139.

Mammucari C, Raffaello A, Vecellio Reane D, Rizzuto R (2016) Molecular structure and pathophysiological roles of the Mitochondrial Calcium Uniporter. Biochim Biophys Acta - Mol Cell Res 1863:2457–2464.

Marchi S, Pinton P (2014) The mitochondrial calcium uniporter complex: molecular components, structure and physiopathological implications. J Physiol 592:829–839.

Mark LP, Prost RW, Ulmer JL, Smith MM, Daniels DL, Strottmann JM, Brown WD, Hacein-Bey L (2001) Pictorial Review of Glutamate Excitotoxicity: Fundamental Concepts for Neuroimaging. Am J Neuroradiol 22:1813 LP – 1824.

Mautes AEM, Weinzierl MR, Donovan F, Noble LJ (2000) Vascular Events After Spinal Cord Injury: Contribution to Secondary Pathogenesis. Phys Ther 80:673–687.

Maynard RL, Downes N (2019) Chapter 4 - Vertebrae, Ribs, Sternum, Pectoral and Pelvic Girdles, and Bones of the Limbs. In (Maynard RL, Downes NBT-A and H of the LR in T and BR, eds), pp 23–39. Academic Press.

McKerracher L, Anderson KD (2013) Analysis of recruitment and outcomes in the phase I/IIa Cethrin clinical trial for acute spinal cord injury. J Neurotrauma 30:1795–1804.

Mendes CS, Bartos I, Márka Z, Akay T, Márka S, Mann RS (2015) Quantification of gait parameters in freely walking rodents. BMC Biol 13:50.

Michael-Titus A, Revest P, Shortland P (2010) 4 - THE SPINAL CORD. In (Michael-Titus A, Revest P, Shortland PBT-TNS (Second E, eds), pp 59–78. Churchill Livingstone.

Mishra J, Jhun BS, Hurst S, O-Uchi J, Csordás G, Sheu S-S (2017) The Mitochondrial Ca(2+) Uniporter: Structure, Function, and Pharmacology. Handb Exp Pharmacol 240:129–156.

Miyasaka K, Asano T, Ushikoshi S, Hida K, Koyanagi I (2000) Vascular anatomy of the spinal cord and classification of spinal arteriovenous malformations. Interv Neuroradiol 6 Suppl 1:195–198.

Molnár E (2018) Glutamate Receptor BT - Encyclopedia of Signaling Molecules. In (Choi S, ed), pp 2138–2146. Cham: Springer International Publishing.

Momeni HR (2011) Role of calpain in apoptosis. Cell J 13:65–72.

Moore CL (1971) Specific inhibition of mitochondrial Ca++ transport by ruthenium red. Biochem Biophys Res Commun 42:298–305.

Murray M, Cooper G, Rodnitzky RL (2003) Organization of the Spinal Cord BT - Neuroscience in Medicine. In (Conn PM, ed), pp 197–216. Totowa, NJ: Humana Press.

Nair X, Watson EL, Luft JH (1975) Effects of ruthenium red and KCl on responses of guinea pig umbilical veins. Eur J Pharmacol 31:327–331.

Nathan SR, Pino NW, Arduino DM, Perocchi F, MacMillan SN, Wilson JJ (2017) Synthetic Methods for the Preparation of a Functional Analogue of Ru360, a Potent Inhibitor of Mitochondrial Calcium Uptake. Inorg Chem 56:3123–3126.

National Research Council (1994) Sharing Laboratory Resources: Genetically Altered Mice. Washington (DC).

Nichols M, Pavlov E V, Robertson GS (2018) Tamoxifen-induced knockdown of the mitochondrial calcium uniporter in Thy1-expressing neurons protects mice from hypoxic/ischemic brain injury. Cell Death Dis 9:606.

Nishi R, Liu H, Chu Y, Hamamura M, Su M-Y, Nalcioglu O, Anderson A (2007) Behavioral, Histological, and Ex Vivo Magnetic Resonance Imaging Assessment of Graded Contusion Spinal Cord Injury in Mice. J Neurotrauma 24:674–689.

Nógrádi A, Vrbová G (n.d.) Anatomy and Physiology of the Spinal Cord. Madame Curie Biosci Database.

Noonan VK, Fingas M, Farry A, Baxter D, Singh A, Fehlings MG, Dvorak MF (2012) Incidence and Prevalence of Spinal Cord Injury in Canada: A National Perspective. Neuroepidemiology 38:219–226.

Novorolsky RJ, Nichols M, Kim JS, Pavlov E V, J Woods J, Wilson JJ, Robertson GS (2020) The cell-permeable mitochondrial calcium uniporter inhibitor Ru265 preserves cortical neuron respiration after lethal oxygen glucose deprivation and reduces hypoxic/ischemic brain injury. J Cereb blood flow Metab Off J Int Soc Cereb Blood Flow Metab 40:1172–1181.

NSCISC (2019) Spinal Cord Injury Facts and Figures at a Glance. Natl Spinal Cord Inj Stat Cent.

O-Uchi J, Jhun BS, Sheu S-S (2014) 7 - Structural and Molecular Bases of Mitochondrial Ion Channel Function. In (Zipes DP, Jalife JBT-CEFC to B (Sixth E, eds), pp 71–84. Philadelphia: W.B. Saunders.

Oladosu FA, Ciszek BP, O'Buckley SC, Nackley AG (2016) Novel intrathecal and subcutaneous catheter delivery systems in the mouse. J Neurosci Methods 264:119–128.

Olsen ML, Sontheimer HBT-RM in BS (2015) Ionic Channels in Glia☆. In. Elsevier.

Ow Y-LP, Green DR, Hao Z, Mak TW (2008) Cytochrome c: functions beyond respiration. Nat Rev Mol Cell Biol 9:532–542.

Oyinbo CA (2011) Secondary injury mechanisms in traumatic spinal cord injury: a nugget of this multiply cascade. Acta Neurobiol Exp (Wars) 71:281–299.

Pakulska MM, Ballios BG, Shoichet MS (2012) Injectable hydrogels for central nervous system therapy. Biomed Mater 7:24101.

Parhi R (2017) Cross-Linked Hydrogel for Pharmaceutical Applications: A Review. Adv Pharm Bull 7:515–530.

Park J, Lee Y, Park T, Kang JY, Mun SA, Jin M, Yang J, Eom SH (2020) Structure of the MICU1-MICU2 heterodimer provides insights into the gatekeeping threshold shift. IUCrJ 7:355–365.

Pinton P, Giorgi C, Siviero R, Zecchini E, Rizzuto R (2008) Calcium and apoptosis: ER-mitochondria Ca2+ transfer in the control of apoptosis. Oncogene 27:6407–6418.

Popa C, Popa F, Grigorean VT, Onose G, Sandu AM, Popescu M, Burnei G, Strambu V, Sinescu C (2010) Vascular dysfunctions following spinal cord injury. J Med Life 3:275–285.

Post MWM, van Leeuwen CMC (2012) Psychosocial issues in spinal cord injury: a review. Spinal Cord 50:382–389.

Praxis Spinal Cord Institute (2021) Rick Hansen Spinal Cord Injury Registry - A look at traumatic spinal cord injury in Canada in 2019. Vancouver, BC.

Purves D, Augustine G, Fitzpatrick D, Katz L, LaMantia A-S, McNamara J, Williams M (2001) Neuroscience, 2nd ed. Massachusetts: Sutherland.

Raguindin PF, Muka T, Glisic M (2021) Sex and gender gap in spinal cord injury research: Focus on cardiometabolic diseases. A mini review. Maturitas 147:14–18.

Ramakonar H, Fehlings MG (2021) 'Time is Spine': new evidence supports decompression within 24 h for acute spinal cord injury. Spinal Cord 59:933–934.

Rawson RL, Yam L, Weimer RM, Bend EG, Hartwieg E, Horvitz HR, Clark SG, Jorgensen EM (2014) Axons degenerate in the absence of mitochondria in C. elegans. Curr Biol 24:760–765.

Roberts TT, Leonard GR, Cepela DJ (2017) Classifications In Brief: American Spinal Injury Association (ASIA) Impairment Scale. Clin Orthop Relat Res 475:1499–1504.

Roderick TH, Wimer RE, Wimer CC, Schwartzkroin PA (1973) Genetic and phenotypic variation in weight of brain and spinal cord between inbred strains of mice. Brain Res 64:345–353.

Rowland JW, Hawryluk GWJ, Kwon B, Fehlings MG (2008) Current status of acute spinal cord injury pathophysiology and emerging therapies: promise on the horizon. Neurosurg Focus 25:E2.

Sasaki S (2010) Determination of altered mitochondria ultrastructure by electron microscopy. Methods Mol Biol 648:279–290.

Saxton WM, Hollenbeck PJ (2012) The axonal transport of mitochondria. J Cell Sci 125:2095–2104.

Sbodio JI, Snyder SH, Paul BD (2019) Redox Mechanisms in Neurodegeneration: From Disease Outcomes to Therapeutic Opportunities. Antioxid Redox Signal 30:1450–1499.

Schmued LC, Albertson C, Slikker W (1997) Fluoro-Jade: a novel fluorochrome for the sensitive and reliable histochemical localization of neuronal degeneration. Brain Res 751:37–46.

Schmued LC, Stowers CC, Scallet AC, Xu L (2005) Fluoro-Jade C results in ultra high resolution and contrast labeling of degenerating neurons. Brain Res 1035:24–31.

Scholpa NE, Schnellmann RG (2017) Mitochondrial-Based Therapeutics for the Treatment of Spinal Cord Injury: Mitochondrial Biogenesis as a Potential Pharmacological Target. J Pharmacol Exp Ther 363:303–313.

Schwartz ED, Falcone SF, Quencer RM, Green BA (1999) Posttraumatic syringomyelia: pathogenesis, imaging, and treatment. AJR Am J Roentgenol 173:487–492.

Sengul G, Watson C (2012) Chapter 13 - Spinal Cord. In (Watson C, Paxinos G, Puelles LBT-TMNS, eds), pp 424–458. San Diego: Academic Press.

Sezer N, Akkuş S, Uğurlu FG (2015) Chronic complications of spinal cord injury. World J Orthop 6:24–33.

Shanti N, Kubeck JP, Vaccaro AR, Raushning W (2007) CHAPTER 5B - Anatomy of the Lumbar Spine. In (Vaccaro AR, Haid RW, Papadopoulos S, Sasso RC, Traynelis VCBT-SA, eds), pp 61–65. Philadelphia: W.B. Saunders.

Sharif-Alhoseini M, Khormali M, Rezaei M, Safdarian M, Hajighadery A, Khalatbari MM, Safdarian M, Meknatkhah S, Rezvan M, Chalangari M, Derakhshan P, Rahimi-Movaghar V (2017) Animal models of spinal cord injury: a systematic review. Spinal Cord 55:714–721.

Shi Y (2004) Caspase activation, inhibition, and reactivation: a mechanistic view. Protein Sci 13:1979–1987.

Shultz RB, Zhong Y (2021) Hydrogel-based local drug delivery strategies for spinal cord repair. Neural Regen Res 16:247–253.

Simmons EC, Scholpa NE, Crossman JD, Schnellmann RG (2022) Chapter 28 - Mitochondrial biogenesis for the treatment of spinal cord injury. In (Rajendram R, Preedy VR, Martin CRBT-D and T of SCI, eds), pp 359–372. Academic Press.

Singh R, Lillard JWJ (2009) Nanoparticle-based targeted drug delivery. Exp Mol Pathol 86:215–223.

Stifani N (2014) Motor neurons and the generation of spinal motor neurons diversity . Front Cell Neurosci 8:293.

Su L-J, Zhang J-H, Gomez H, Murugan R, Hong X, Xu D, Jiang F, Peng Z-Y (2019) Reactive Oxygen Species-Induced Lipid Peroxidation in Apoptosis, Autophagy, and Ferroptosis. Oxid Med Cell Longev 2019:5080843.

Sun Y, Du L, Yang M, Li Q, Jia X, Li Q, Zhu L, Zhang Y, Liu Y, Liu S (2021) Brain-targeted drug delivery assisted by physical techniques and its potential applications in traditional Chinese medicine. J Tradit Chinese Med Sci 8:186–197.

Tang C, Cai J, Yin X-M, Weinberg JM, Venkatachalam MA, Dong Z (2021) Mitochondrial quality control in kidney injury and repair. Nat Rev Nephrol 17:299–318.

Tator CH, Fehlings MG (1991) Review of the secondary injury theory of acute spinal cord trauma with emphasis on vascular mechanisms. J Neurosurg 75:15–26.

Thau L, Reddy V, Singh P (2021) Anatomy, Central Nervous System. Treasure Island, FL: StatPearls Publishing.

Thomas C, Grumbles R (2014) Age at spinal cord injury determines muscle strength . Front Integr Neurosci 8.

Turrens JF (2003) Mitochondrial formation of reactive oxygen species. J Physiol 552:335–344.

Uchiyama A, Kim JS, Kon K, Jaeschke H, Ikejima K, Watanabe S, Lemasters JJ (2008) Translocation of iron from lysosomes into mitochondria is a key event during oxidative stress-induced hepatocellular injury. Hepatology 48:1644–1654.

Vandenberg RJ, Ryan RM (2013) Mechanisms of Glutamate Transport. Physiol Rev 93:1621–1657.

Velasco I, Morán J, Tapia R (1995) Selective neurotoxicity of ruthenium red in primary cultures. Neurochem Res 20:599–604.

Vertex Pharmaceuticals Incorporated (2007) A Safety Study for Cethrin (BA-210) in the Treatment of Acute Thoracic and Cervical Spinal Cord Injuries.

Wada N, Shimizu T, Takai S, Shimizu N, Kanai AJ, Tyagi P, Kakizaki H, Yoshimura N (2017) Post-injury bladder management strategy influences lower urinary tract dysfunction in the mouse model of spinal cord injury. Neurourol Urodyn 36:1301–1305.

Watson C, Harrison M (2012) The Location of the Major Ascending and Descending Spinal Cord Tracts in all Spinal Cord Segments in the Mouse: Actual and Extrapolated. Anat Rec (Hoboken) 295:1692–1697.

Watson C, Kayalioglu G (2009) Chapter 1 - The Organization of the Spinal Cord. In (Watson C, Paxinos G, Kayalioglu GBT-TSC, eds), pp 1–7. San Diego: Academic Press.

Watson SA, McStay GP (2020) Functions of Cytochrome c oxidase Assembly Factors. Int J Mol Sci 21:7254.

Waxenbaum JA, Reddy V, Williams C, Futterman B (2021) Anatomy, Back, Lumbar Vertebrae. In. Treasure Island (FL).

Wen H, Jung H, Li X (2015) Drug Delivery Approaches in Addressing Clinical Pharmacology-Related Issues: Opportunities and Challenges. AAPS J 17:1327–1340.

Whetstone WD, Hsu J-YC, Eisenberg M, Werb Z, Noble-Haeusslein LJ (2003) Blood-spinal cord barrier after spinal cord injury: relation to revascularization and wound healing. J Neurosci Res 74:227–239.

Woods JJ, Lovett J, Lai B, Harris HH, Wilson JJ (2020) Redox Stability Controls the Cellular Uptake and Activity of Ruthenium-Based Inhibitors of the Mitochondrial Calcium Uniporter (MCU). Angew Chem Int Ed Engl 59:6482–6491.

Woods JJ, Nemani N, Shanmughapriya S, Kumar A, Zhang M, Nathan SR, Thomas M, Carvalho E, Ramachandran K, Srikantan S, Stathopulos PB, Wilson JJ, Madesh M (2019) A Selective and Cell-Permeable Mitochondrial Calcium Uniporter (MCU) Inhibitor Preserves Mitochondrial Bioenergetics after Hypoxia/Reoxygenation Injury. ACS Cent Sci 5:153–166.

Xu R, Burgar A, Ebraheim NA, Yeasting RA (1999) The quantitative anatomy of the laminas of the spine. Spine (Phila Pa 1976) 24:107–113.

Xu W, Chi L, Xu R, Ke Y, Luo C, Cai J, Qiu M, Gozal D, Liu R (2005) Increased production of reactive oxygen species contributes to motor neuron death in a compression mouse model of spinal cord injury. Spinal Cord 43:204–213.

Yang T, Dai Y, Chen G, Cui S (2020) Dissecting the Dual Role of the Glial Scar and Scar-Forming Astrocytes in Spinal Cord Injury . Front Cell Neurosci 14.

Ying WL, Emerson J, Clarke MJ, Sanadi DR (1991) Inhibition of mitochondrial calcium ion transport by an oxo-bridged dinuclear ruthenium ammine complex. Biochemistry 30:4949–4952.

Young W (2002) Chapter 17 Spinal cord contusion models. In: Spinal Cord Trauma: Regeneration, Neural Repair and Functional Recovery (McKerracher L, Doucet G, Rossignol SBT-P in BR, eds), pp 231–255. Elsevier.

Zhang L, Wang H, Zhou X, Mao L, Ding K, Hu Z (2019) Role of mitochondrial calcium uniporter-mediated Ca2+ and iron accumulation in traumatic brain injury. J Cell Mol Med 23:2995–3009.

Zhang M, Zheng J, Nussinov R, Ma B (2017) Release of Cytochrome C from Bax Pores at the Mitochondrial Membrane. Sci Rep 7:2635.

Zhang N, Fang M, Chen H, Gou F, Ding M (2014) Evaluation of spinal cord injury animal models. Neural Regen Res 9:2008–2012.

Zhou Y, Danbolt NC (2014) Glutamate as a neurotransmitter in the healthy brain. J Neural Transm 121:799–817.

Zorov DB, Juhaszova M, Sollott SJ (2014) Mitochondrial reactive oxygen species (ROS) and ROS-induced ROS release. Physiol Rev 94:909–950.

APPENDIX

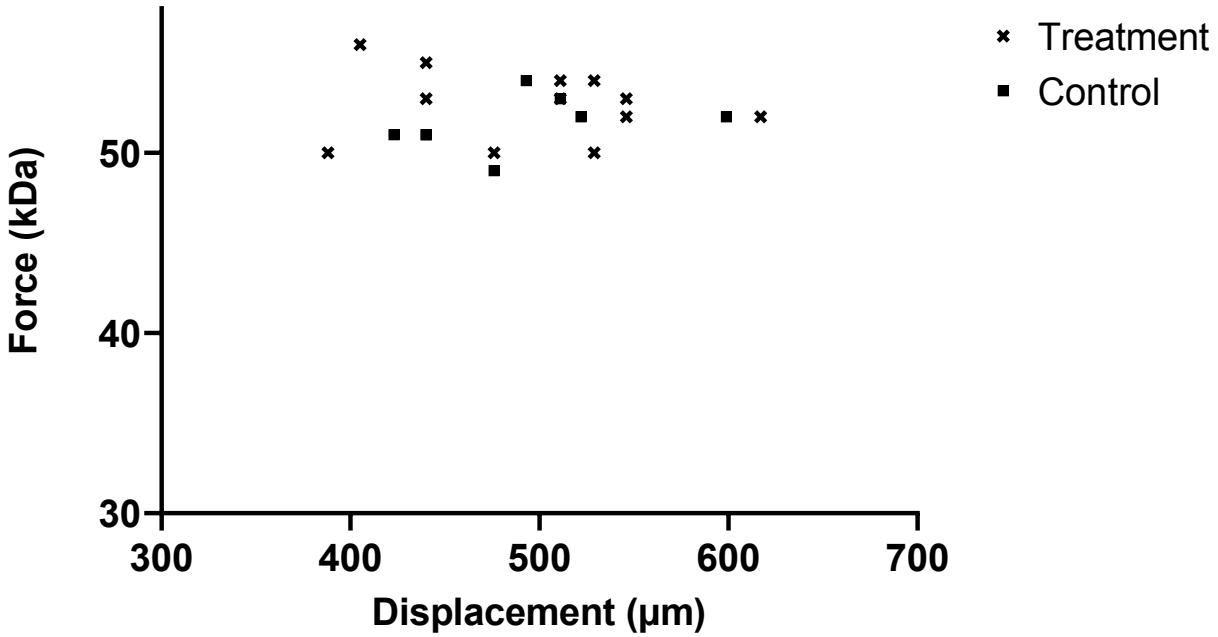

Figure 23: Impact parameters from control and treatment mice used in mitoprotection and neuroprotection experiments. Injury severity is a factor of both force and displacement.

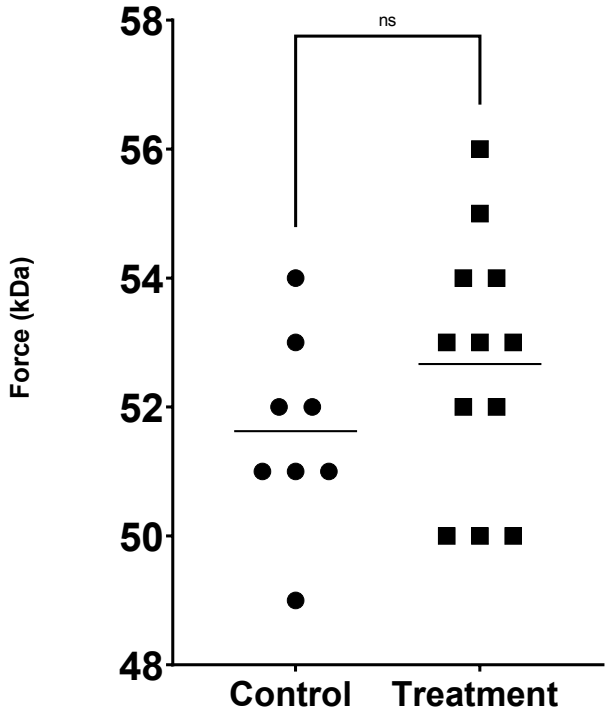

***Figure 24**:* Force (kDa) for control and Ru265 treated animals used in experiments. Horizontal lines represent the mean. (t(18)=1.265, p=0.2218, two-tailed).

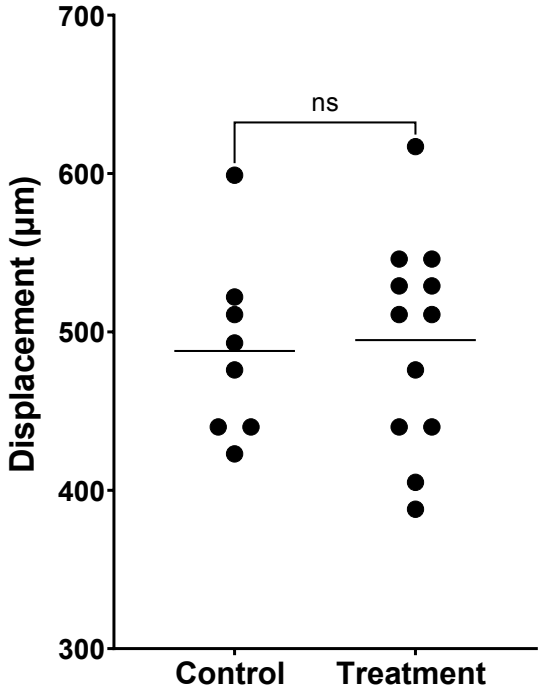

***Figure 25**:* Displacement (µm) for control and Ru265 treated animals used in experiments. Horizontal lines represent the mean. (t(18)=0.2369, p=0.8154, two-tailed).

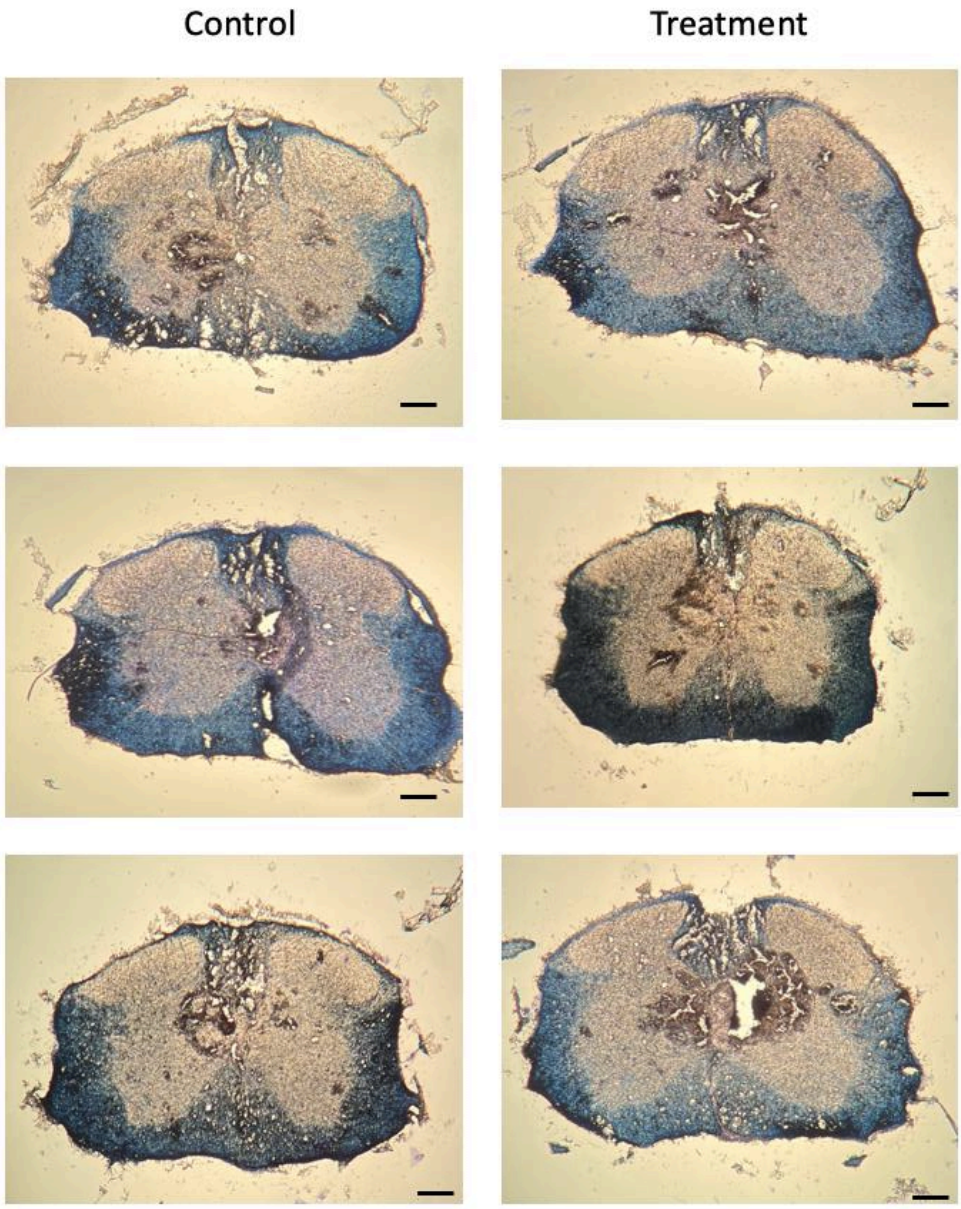

Figure 26: Histology of representative injured spinal cord samples in 3 control and 3 Ru265 treated animals stained using Eriochrome cyanine R. Scale Bar=200 µm.